The Astrophysical Journal, 836:167 (30pp), 2017 February 20 https://doi.org/10.3847/1538-4357/836/2/167

Characterizing K2 Candidate Planetary Systems Orbiting Low-mass Stars. I. Classifying Low-mass Host Stars Observed during Campaigns 1–7

Courtney D. Dressing[1,8], Elisabeth R. Newton[2,9], Joshua E. Schlieder[3,5], David Charbonneau[4], Heather A. Knutson[1], Andrew Vanderburg[4,10], and Evan Sinukoff[6,7]
[1] Division of Geological & Planetary Sciences, California Institute of Technology, Pasadena, CA 91125, USA; dressing@caltech.edu
[2] Department of Physics, Massachusetts Institute of Technology, Cambridge, MA 02139, USA
[3] IPAC-NExScI, California Institute of Technology, Pasadena, CA 91125, USA
[4] Harvard-Smithsonian Center for Astrophysics, Cambridge, MA 02138, USA
[5] NASA Goddard Space Flight Center, Greenbelt, MD 20771, USA
[6] Institute for Astronomy, University of Hawaí at Mānoa, Honolulu, HI 96822, USA
[7] Cahill Center for Astrophysics, California Institute of Technology, 1216 East California Boulevard, Pasadena, CA 91125, USA
Received 2016 September 5; revised 2016 November 17; accepted 2016 November 18; published 2017 February 17

Abstract

We present near-infrared spectra for 144 candidate planetary systems identified during Campaigns 1–7 of the NASA K2 Mission. The goal of the survey was to characterize planets orbiting low-mass stars, but our Infrared Telescope Facility/SpeX and Palomar/TripleSpec spectroscopic observations revealed that 49% of our targets were actually giant stars or hotter dwarfs reddened by interstellar extinction. For the 72 stars with spectra consistent with classification as cool dwarfs (spectral types K3–M4), we refined their stellar properties by applying empirical relations based on stars with interferometric radius measurements. Although our revised temperatures are generally consistent with those reported in the Ecliptic Plane Input Catalog (EPIC), our revised stellar radii are typically 0.13 $R_{\odot}$ (39%) larger than the EPIC values, which were based on model isochrones that have been shown to underestimate the radii of cool dwarfs. Our improved stellar characterizations will enable more efficient prioritization of K2 targets for follow-up studies.

Key words: planetary systems – planets and satellites: fundamental parameters – stars: fundamental parameters – stars: late-type – stars: low-mass – techniques: spectroscopic

1. Introduction

Beginning in 2009, the NASA *Kepler* mission revolutionized exoplanet science by searching for planets transiting roughly 190,000 stars and detecting thousands of planet candidates (Borucki et al. 2010, 2011a, 2011b; Batalha et al. 2013; Burke et al. 2014). The main *Kepler* mission ended in 2013 when the second of four reaction wheels failed, thereby destroying the ability of the spacecraft to point stably. Although the two-wheeled *Kepler* was not able to continue observing the original targets, Ball Aerospace engineers and *Kepler* team members realized that the torque from solar pressure could be mitigated by selecting fields along the ecliptic plane. In this new mode of operation (known as the K2 Mission), the spacecraft stares at 10,000–30,000 stars per field for roughly 80 days before switching to another field along the ecliptic (Howell et al. 2014; Van Cleve et al. 2016). Unlike in the original *Kepler* mission, all K2 targets are selected from community-driven Guest Observer (GO) proposals.

The K2 mission design is particularly well-matched for studies of planetary systems orbiting low-mass stars. Although M dwarfs are intrinsically fainter than Sun-like stars, the prevalence of M dwarfs within the Galaxy (e.g., Henry et al. 2006; Winters et al. 2015) ensures that there are several thousand reasonably bright low-mass stars per K2 field. Due to their smaller sizes and cooler temperatures, these stars are relatively easy targets for planet detection for two main reasons. First, the transit depth is deeper for a given planet radius. Second, the habitable zones are closer to the stars, thereby increasing both the geometric likelihood that planets within the habitable zone will appear to transit and the number of transits that could be observed during a single K2 campaign. For the coolest low-mass stars, the orbital periods of planets within the habitable zone are even short enough that potentially habitable planets would transit multiple times per campaign.

The "Small Star Advantage" of deeper transit depths and higher transit probabilities within the habitable zone is partially offset by the challenge of identifying samples of low-mass stars for observation. When preparing for the original *Kepler* mission, Brown et al. (2011) conducted an extensive survey of the proposed field of view to identify advantageous targets and determine rough stellar properties. In contrast, the planning cycle for the K2 mission was too fast-paced to allow for such methodical preparation. During the early days of the K2 mission, the official Ecliptic Plane Input Catalog (EPIC) contained only coordinates, photometry, proper motions, and, when available, parallaxes. Proposers therefore had to use their own knowledge of stellar astrophysics to determine which stars were suitable for their investigations.

More recently, Huber et al. (2016) updated the EPIC to include stellar properties for 138,600 stars. After completing the messy tasks of matching sources from multiple catalogs, converting the photometry to standard systems, and enforcing quality cuts to discard low-quality photometry, Huber et al. (2016) used the *Galaxia* galactic model (Sharma et al. 2011) to generate synthetic realizations of different K2 fields. They then determined the most likely parameters for each K2 target star, given the available photometric and kinematic information.

[8] NASA Sagan Fellow.
[9] National Science Foundation Astronomy & Astrophysics Postdoctoral Fellow.
[10] National Science Foundation Graduate Research Fellow.

Table 1
Observing Conditions

Semester	Instru	Program	Date (UT)	Seeing	Weather Conditions	*K2* Targets[a]
2015A	SpeX	989	2015 Apr 16	0.″7–1.″0	Clear	2[b]
	SpeX	989	2015 May 5	0.″3–0.″8	Light wind, clear	5[c]
	SpeX	981	2015 Jun 13	0.″3–1.″0	Cirrus, patchy clouds	2[d]
2015B	SpeX	057, 068	2015 Aug 7	0.″5–1.″0	Clear at start; closed early due to high humidity	3[e]
	SpeX	068	2015 Sep 24	0.″5–1.″0	Patchy clouds cleared slightly overnight	20
	SpeX	072	2015 Oct 14	0.″4–1.″0	Cirrus	1[f]
	SpeX	068	2015 Nov 26	0.″5–2.″0	Patchy clouds; high humidity	16
	SpeX	068	2015 Nov 27	0.″6	Cirrus	16
2016A	TSPEC	P08	2016 Feb 19	1.″2–2.″0	Cirrus clouds at start; moderately cloudy by morning	3
	SpeX	066	2016 Mar 4	0.″5–1.″0	Clear	10
	SpeX	066	2016 Mar 8	0.″5–1.″0	Thick, patchy clouds at sunset; thinner clouds by morning	12
	SpeX	986	2016 Mar 10	0.″9	Cirrus	5[g]
	TSPEC	P08	2016 Mar 27	0.″9	Clear	15
	TSPEC	P08	2016 Mar 28	0.″9–2.″1	Patchy clouds; closed early due to high humidity and fog	9
	TSPEC	P08	2016 Apr 18	1.″1–1.″9	Clear	11
	SpeX	066	2016 May 5	0.″5–1.″0	Patchy clouds	11
	SpeX	066	2016 May 6	0.″3–0.″9	Clear	6
	SpeX	066	2016 Jun 7	0.″4–1.″0	Clear	8
2016B	SpeX	057	2016 Oct 26	0.″5–1.″4	Clear	5

Notes.
[a] We observed some stars twice on two different nights to assess the repeatability of our analysis.
[b] Night awarded to Andrew Howard.
[c] Night awarded to Andrew Howard, but observations obtained by Joshua Schlieder.
[d] Observations obtained by Evan Sinukoff.
[e] Includes one observation acquired by Will Best (Program 057) and two acquired by Courtney Dressing (Program 068).
[f] Observations obtained by Kimberly Aller.
[g] Night awarded to Andrew Howard, but observations obtained by Courtney Dressing.

Table 2
Targets Observed by the *K2* Campaign

Campaign				Total	Classification in This Paper		
Field Number	R.A. (hh:mm:ss)	Decl. (dd:mm:ss)	Galactic Latitude (°)	Targets Observed	Cool Dwarfs[a]	Hotter Dwarfs	Giants
1	11:35:46	+01:25:02	+59	10	9 (90%)	1 (10%)	0 (0%)
2	16:24:30	−22:26:50	+19	8	0 (0%)	4 (50%)	4 (50%)
3	22:26:40	−11:05:48	−52	12	6 (50%)	5 (42%)	1 (8%)
4	03:56:18	+18:39:38	−26	24	10 (42%)	10 (42%)	4 (17%)
5	08:40:38	+16:49:47	+32	41	27 (66%)	13 (32%)	1 (2%)
6	13:39:28	−11:17:43	+50	34	16 (47%)	12 (36%)	6 (18%)
7	19:11:19	−23:21:36	−15	17	6 (35%)	4 (24%)	7 (41%)
1–7	…	…	…	146	74 (51%)	49 (34%)	23 (16%)

Note.
[a] Two *K2* targets (EPIC 211694226 and EPIC 212773309) have nearby companions that may or may not be physically associated. We classified 74 cool dwarfs in 72 systems.

When possible, the analysis also incorporated *Hipparcos* parallaxes (van Leeuwen 2007) and spectroscopic estimates of $T_{\rm eff}$, $\log g$, and [Fe/H] from RAVE DR4 (Kordopatis et al. 2013), LAMOST DR1 (Luo et al. 2015), and APOGEE DR12 (Alam et al. 2015).

In all cases, *Galaxia* used Padova isochrones (Girardi et al. 2000; Marigo & Girardi 2007; Marigo et al. 2008) to determine stellar properties. Aware that these isochrones tend to underpredict the radii of low-mass stars (Boyajian et al. 2012), Huber et al. (2016) therefore warned that the EPIC radii of low-mass stars may be up to roughly 20% too small. Given that 41% of selected K2 targets are low-mass M and K dwarfs (Huber et al. 2016), improving the radius estimates of low-mass K2 targets is important for maximizing the scientific yield of the K2

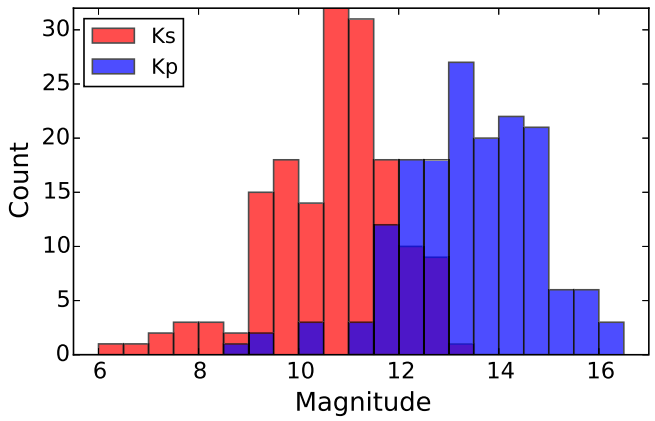

Figure 1. Magnitude distribution of our full target sample in the *Kepler* bandpass (*Kp*; blue) and *Ks* (red). Our targets have median brightnesses of $Ks = 10.8$ and $Kp = 13.5$. The *Kepler* bandpass extends from roughly 420 nm to 900 nm with maximum response at 575 nm (Van Cleve & Caldwell 2016); the *Ks* bandpass is centered at 2.159 μm (Cohen et al. 2003).

mission. Both accurate characterization of individual planet candidates and ensemble studies of planetary occurrence demand reliable stellar properties.

Even during the more methodical *Kepler* era, the properties of low-mass targets were frequently revised. Initially, Brown et al. (2011) characterized all of the targets by comparing multi-band photometry to Castelli & Kurucz (2004) stellar models. This approach worked well for characterizing Sun-like stars, but Brown et al. (2011) cautioned that the *Kepler* Input Catalog (KIC) temperatures were untrustworthy for stars cooler than 3750 K. Batalha et al. (2013) later improved the classifications for many *Kepler* targets by replacing the original KIC values with parameters of the nearest model star selected from Yonsei-Yale isochrones (Demarque et al. 2004), but those models noticeably underpredict the radii of low-mass stars (Boyajian et al. 2012).

Considering the non-planet candidate host stars, Mann et al. (2012) acquired medium-resolution ($1150 \lesssim R \lesssim 2300$) visible spectra of 382 putative low-mass dwarf targets. Using those stars as a "training set," they found that the vast majority ($96\% \pm 1\%$) of cool, bright ($Kp < 14$) *Kepler* target stars were actually giants. For fainter cool stars, giant contamination was much less pronounced ($7\% \pm 3\%$). For stars that were correctly classified as dwarfs, Mann et al. (2012) found that the KIC temperatures were systematically 110 K hotter than the values determined by comparing their spectra to the BT-SETTL series of PHOENIX stellar models (Allard et al. 2011).

In a following paper, Mann et al. (2013b) obtained optical spectra of 123 putative low-mass stars hosting 188 planet candidates and NIR spectra for a smaller subset of host stars. Flux-calibrating their spectra and comparing them to BT-SETTL stellar models, they derived a set of empirically based relations to determine stellar effective temperatures from spectral indices measured at visible and near-infrared wavelengths. Mann et al. (2013b) also introduced a set of temperature–radius, temperature–mass, and temperature–luminosity relations based on the sample of stars with well-constrained radii, effective temperatures, and bolometric fluxes.

Focusing specifically on the coolest *Kepler* targets, Muirhead et al. (2012) re-characterized 84 cool *Kepler* Object of Interest (KOI) host stars by obtaining near-infrared spectra with TripleSpec at the Palomar Hale Telescope. As explained in Rojas-Ayala et al. (2012), they estimated temperatures and metallicities using the H_2O-K2 index and the equivalent widths (EW) of the Na I line at 2.210 μm and the Ca I line at 2.260 μm. Depending on stellar metallicity, the H_2O-K2 index saturates at approximately 3900 K, so this approach cannot be used to characterize mid-K dwarfs. Muirhead et al. (2012) then interpolated the temperatures and metallicities onto Dartmouth isochrones (Dotter et al. 2008; Feiden et al. 2011) to estimate the radii and masses of their target stars. In a follow-up analysis, Muirhead et al. (2014) expanded their sample to 103 cool KOI host stars and updated their mass and radius estimates using newer versions of the Dartmouth isochrones.

Both KOIs and non-KOIs need to be accurately characterized in order to use the *Kepler* data to investigate planet occurrence rates, which motivated Dressing & Charbonneau (2013) to refit the KIC photometry using Dartmouth Stellar Evolutionary Models (Dotter et al. 2008; Feiden et al. 2011) to determine revised properties for 3897 dwarfs cooler than 4000 K. We then used the revised stellar properties to investigate the frequency of planetary systems orbiting low-mass stars.

Recognizing that the stellar parameters inferred in the previous studies were based on stellar models and were therefore likely to underestimate stellar radii, Newton et al. (2015) revised the properties of cool KOI host stars by employing empirical relations based on interferometrically characterized stars. Specifically, Newton et al. (2015) established relationships between the EWs of Mg and Al features in *H*-band spectra from Infrared Telescope Facility (IRTF)/SpeX and the temperatures, luminosities, and radii of low-mass stars. Newton et al. (2015) found that the radii of M dwarf planet candidates were typically 15% larger than previously estimated in the Huber et al. (2014) catalog, which contained a compilation of results from previous studies, including Dressing & Charbonneau (2013), Muirhead et al. (2012, 2014), and Mann et al. (2013b).

Accounting for the systematic effect of previously underestimated stellar radii, Dressing & Charbonneau (2015) investigated low-mass star planet occurrence in more detail by employing their own pipeline to detect candidates and measure search completeness. Using the full four-year *Kepler* data set, we found that the mean number of small (0.5–4 $R_\oplus$) planets per late K or early M dwarf is 2.5 ± 0.2 planets per star for orbital periods shorter than 200 days. Within the habitable zone, we estimated occurrence rates of $0.24^{+0.18}_{-0.08}$ Earth-size planets and $0.21^{+0.11}_{-0.06}$ super-Earths (1.5–2 $R_\oplus$) per star. Those estimates agree well with rates derived in independent studies (e.g., Gaidos 2013; Gaidos et al. 2014, 2016; Morton & Swift 2014).

In order to use the K2 data to conduct similar studies of planet occurrence rates and possibly investigate how the frequency of planetary systems orbiting low-mass stars varies as a function of stellar mass, metallicity, or multiplicity, we first need to characterize the stellar sample. In this paper, we classify the subset of K2 target stars that appear to be low-mass stars harboring planetary systems. In the second paper in this series (C. D. Dressing et al. 2017, in preparation), we use our new stellar classifications to revise the properties of the

Table 3
Observations of *K2* Targets Classified as Giant Stars

EPIC	Observation		Spectral Type[a]	Campaign	EPIC Classification					
	Date	Instru			$T_{\rm eff}$ (K)	ep_$T_{\rm eff}$	em_$T_{\rm eff}$	log g (cgs)	ep_log g	em_log g
202710713	2015 Aug 07	SpeX	K4III	2	3817	92	92	0.523	0.168	0.168
203485624	2016 Jun 7	SpeX	F2III	2	6237	449	187	3.848	0.228	0.020
203776696	2016 Mar 27	TSPEC	F8III	2	6113	1219	508	4.143	0.270	0.315
205064326	2016 Jun 7	SpeX	K0III	2	4734	75	75	2.946	0.144	0.144
206049452	2015 Sep 24	SpeX	M2III	3	4553	191	109	4.671	0.035	0.042
210769880	2015 Sep 24	SpeX	K2III	4	4018	118	802	4.809	2.400	0.060
210843708	2015 Sep 24	SpeX	K3III	4	4823	120	90	2.456	0.075	0.450
211098117	2015 Sep 24	SpeX	K0III	4	3858	186	186	4.870	0.070	0.084
211106187	2015 Nov 27	SpeX	G5III	4	5321	96	192	4.561	0.164	0.020
211351816	2015 Nov 27	SpeX	K2III	5	4742	96	76	2.984	0.483	0.345
212311834	2016 Apr 18	TSPEC	M1III	6	5199	156	188	3.631	0.890	0.890
212443457	2016 Mar 8	SpeX	K0III	6	4804	144	173	4.598	0.025	0.030
212443457	2016 Jun 7	SpeX	K0III	6	4804	144	173	4.598	0.025	0.030
212473154	2016 Jun 7	SpeX	K0III	6	4570	136	136	2.365	0.682	0.186
212586030	2016 Mar 8	SpeX	K1III	6	4814	76	76	3.328	0.144	0.144
212644491	2016 Apr 18	TSPEC	K1III	6	4940	96	96	2.505	0.306	0.663
212786391	2016 Mar 27	TSPEC	G5III	6	4688	109	73	2.164	0.912	0.570
214629283	2016 May 5	SpeX	M3III	7	3508	150	150	0.241	0.310	0.558
214799621	2016 May 5	SpeX	K4III	7	4375	132	132	2.184	0.360	0.216
215030652	2016 Jun 7	SpeX	M0III	7	3935	79	79	0.778	0.250	0.300
215090200	2016 May 5	SpeX	K0III	7	4596	115	172	2.422	0.145	0.203
215174656	2016 May 6	SpeX	K7III	7	3814	92	115	0.538	0.150	0.150
215346008	2016 Jun 7	SpeX	K4III	7	4038	165	132	1.357	1.216	0.228
218006248	2016 May 5	SpeX	M2III	7	3330	33	33	0.088	0.070	0.182

Note.
[a] Spectral types are coarse assignments based on visual inspection of the near-infrared spectra collected in this paper. The assigned spectral types have errors of roughly ±1 subtype. (See Section 4.1 for details.)

associated planet candidates and identify intriguing systems for follow-up analyses.

In Section 2, we describe our observation procedures and conditions. We then discuss the target sample in Section 3 and explain our data reduction and stellar characterization procedures in Section 4. Finally, we address the implications of our results and conclude in Section 5.

2. Observations

We conducted our observations using the SpeX instrument on the NASA Infrared Telescope Facility (IRTF) over 15 partial nights during the 2015A, 2015B, 2016A, and 2016B semesters and the TripleSpec instrument on the Palomar 200″ over four full nights during the 2016A semester. Of our IRTF/SpeX nights, 11 were awarded to C. Dressing via programs 2015B068, 2016A066, and 2016B057; the remaining SpeX time was provided by K. Aller, W. Best, A. Howard, and E. Sinukoff. All of our Palomar time was awarded to C. Dressing for program P08.

As detailed in Table 1, our observing conditions varied from photometric nights to nights with significant cloud cover through which only our brightest targets were observable. As recommended by Vacca et al. (2003), we removed telluric features from our science spectra using observations of A0V stars acquired under similar observing conditions. Accordingly, we interspersed our science observations with observations of nearby A0V stars. When possible, these A0V stars were within 15° of our target stars and observed within one hour at similar airmasses (difference <0.1 airmasses).

2.1. IRTF/SpeX

For our SpeX observations, we selected the 0.″3 × 15″ slit and observed in SXD mode to obtain moderate resolution ($R \approx 2000$) spectra (Rayner et al. 2003, 2004). Due the SpeX upgrade in 2014, our spectra include enhanced wavelength coverage from 0.7 to 2.55 μm.

We carried out all of our observations using an ABBA nod pattern with the default settings of 7.″5 separation between positions A and B and 3.″75 separation between either pointing and the ends of the slit. For all targets except close binary stars, we aligned the slit with the parallactic angle to minimize systematic effects in our reduced spectra; for binary stars, we rotated the slit so that the sky spectra acquired in the B position would be free of contamination from the second star or so that spectra from both stars could be captured simultaneously. We scaled the exposure times for our targets and repeated the ABBA nod pattern as required so that the resulting spectra would have S/N of 100–200 per resolution element.

We calibrated these spectra by running the standardized IRTF calibration sequence every few hours during our observations and ensuring that each region of the sky had a separate set of calibration frames. The calibration sequence includes flats taken using an internal quartz lamp and wavelength calibration spectra acquired using an internal thorium–argon lamp.

2.2. Palomar/TripleSpec

We acquired our TripleSpec observations using the fixed 1″ × 30″ slit, which yields simultaneous coverage between 1.0

Table 4
Observations of *K2* Targets Classified as Hotter Dwarfs

EPIC	Observation		Spectral Type[a]	Campaign	EPIC Classification					
	Date	Instru			$T_{\rm eff}$ (K)	ep_$T_{\rm eff}$	em_$T_{\rm eff}$	log g (cgs)	ep_log g	em_log g
201754305	2015 Jun 13	SpeX	K3V[b]	1	4755	113	113	4.642	0.045	0.045
204890128	2016 Mar 27	TSPEC	K2V	2	5213	188	707	3.848	0.535	0.535
205084841	2016 Mar 27	TSPEC	K0V	2	4793	207	207	2.369	0.205	0.656
205145448	2016 Jun 7	SpeX	G5V	2	5700	390	57	3.841	1.362	0.020
205145448	2016 May 5	SpeX	G5V	2	5700	390	57	3.841	1.362	0.020
205686202	2016 May 5	SpeX	K1V	2	3809	68	1432	4.889	0.399	0.084
206055981	2016 Oct 26	SpeX	K3V[b]	3	4522	45	73	4.668	0.028	0.024
206055981	2015 Nov 26	SpeX	K3V[b]	3	4522	45	73	4.668	0.028	0.024
206056433	2016 Oct 26	SpeX	K4V[b]	3	4506	109	54	4.666	0.025	0.045
206056433	2015 Nov 26	SpeX	K4V[b]	3	4506	109	54	4.666	0.025	0.045
206096602	2015 Aug 07	SpeX	K3V[b]	3	4617	138	138	4.649	0.030	0.036
206096602	2015 Sep 24	SpeX	K3V[b]	3	4617	138	138	4.649	0.030	0.036
206135267	2015 Sep 24	SpeX	K2V	3	5165	123	215	3.678	0.286	0.130
206144956	2015 Sep 24	SpeX	K2V	3	4848	78	97	4.611	0.025	0.025
210414957[c]	2015 Nov 26	SpeX	G2V	4	5404	107	86	3.779	0.196	0.020
210423938	2015 Nov 27	SpeX	K3V[b]	4	4856	114	171	2.876	0.582	0.485
210577548	2015 Nov 26	SpeX	K2V	4	…	…	…	…	…	…
210609658	2015 Sep 24	SpeX	K2V	4	4963	97	97	3.268	0.416	0.260
210731500	2015 Nov 27	SpeX	K1V	4	5406	168	168	4.472	0.476	0.068
210754505	2015 Nov 26	SpeX	G5V	4	6041	120	120	4.224	0.168	0.140
210793570	2015 Nov 26	SpeX	K3V[b]	4	4896	118	118	3.242	0.609	0.435
210852232	2015 Nov 27	SpeX	K0V	4	5437	167	301	4.527	0.384	0.040
211058748	2015 Nov 27	SpeX	K2V	4	5070	81	243	4.615	0.060	0.110
211133138	2015 Nov 26	SpeX	K2V	4	5742	367	275	3.965	0.150	0.500
211418290	2015 Nov 27	SpeX	G5V	5	5182	126	126	2.461	0.055	1.111
211529065	2016 Mar 28	TSPEC	K4V[b]	5	4742	167	167	4.621	0.036	0.030
211579683	2016 Mar 28	TSPEC	K3V[b]	5	4829	57	76	3.432	1.045	1.254
211619879	2016 Mar 4	SpeX	K3V[b]	5	4403	303	216	4.706	0.045	0.081
211779390	2015 Nov 26	SpeX	K3V[b]	5	4472	122	87	4.705	0.065	0.195
211783206	2016 Mar 28	TSPEC	K5V[b]	5	4855	94	94	3.324	0.655	1.310
211796070	2016 Mar 4	SpeX	K3V[b]	5	4564	91	91	4.665	0.025	0.035
211797637	2016 Mar 27	TSPEC	K5V[b]	5	4521	108	135	4.696	0.055	0.121
211913977	2015 Nov 27	SpeX	K3V[b]	5	4825	58	77	4.607	0.025	0.040
211970147	2016 Mar 8	SpeX	K3V[b]	5	4576	54	72	4.667	0.035	0.025
212012119	2015 Nov 27	SpeX	K3V[b]	5	4837	78	58	3.178	0.715	0.325
212132195	2015 Nov 27	SpeX	K3V[b]	5	4631	75	112	4.656	0.036	0.020
212138198	2015 Nov 27	SpeX	K3V[b]	5	4975	99	139	4.577	1.218	0.030
212315941	2016 Mar 28	TSPEC	K3V[b]	6	4909	78	118	4.628	0.025	0.040
212470904	2016 Mar 8	SpeX	K5V[b]	6	4761	97	97	4.617	0.042	0.030
212521166[d]	2016 Mar 10	SpeX	K2V	6	4841	145	174	4.628	0.030	0.025
212525174	2016 Mar 27	TSPEC	K4V[b]	6	4163	41	100	4.876	0.084	0.020
212530118	2016 Mar 4	SpeX	K5V[b]	6	4175	41	49	4.824	0.045	0.108
212532636	2016 Mar 28	TSPEC	K3V[b]	6	4519	109	73	4.698	0.030	0.042
212572439	2016 Mar 10	SpeX	K2V	6	4972	59	49	4.593	0.020	0.039
212572439	2016 Mar 27	TSPEC	K2V	6	4972	59	49	4.593	0.020	0.039
212730483	2016 Mar 4	SpeX	K3V[b]	6	4612	55	55	4.657	0.040	0.020
212737443	2016 Mar 28	TSPEC	K3V[b]	6	4542	298	149	4.708	0.040	0.088
212756297	2016 Mar 10	SpeX	K5V[b]	6	4429	78	131	4.729	0.078	0.104
212757039	2016 Apr 18	TSPEC	K1V	6	5510	223	223	4.574	0.088	0.066
212779596	2016 Jun 7	SpeX	K5V[b]	6	4731	77	77	4.623	0.036	0.036
212779596	2016 Mar 8	SpeX	K5V[b]	6	4731	77	77	4.623	0.036	0.036
214173069	2016 Oct 26	SpeX	K3V[b]	7	4659	150	75	4.633	0.035	0.025
214173069	2016 May 6	SpeX	K3V[b]	7	4659	150	75	4.633	0.035	0.025
216111905	2016 May 6	SpeX	G8V	7	5221	126	84	4.543	0.760	0.040
217192839	2016 May 6	SpeX	K2V	7	4563	89	107	4.682	0.042	0.133
219114906	2016 May 6	SpeX	K2V	7	4523	108	90	4.662	0.030	0.042

Notes.
[a] Spectral types are coarse assignments based on visual inspection of the near-infrared spectra collected in this paper. The assigned spectral types have errors of roughly ±1 subtype. (See Section 4.1 for details.)
[b] In general, we list stars with spectral types of K3V or later in the cool dwarf sample rather than the hotter dwarf sample. However, these stars had estimated temperatures >4800 K or estimated radii >0.8 $R_\odot$, which are beyond the validity range of the Newton et al. (2015) relations.
[c] Possible fainter nearby star identified in the Gemini AO image acquired by D. Ciardi (https://exofop.ipac.caltech.edu/k2/edit_target.php?id=210414957).
[d] Characterized by Osborn et al. (2016) as a K3 dwarf with $M_\star = 0.739 \pm 0.017\ M_\odot$, $R_\star = 0.713 \pm 0.020\ R_\odot$, $T_{\rm eff} = 5010 \pm 48$ K, and [Fe/H] $= -0.343 \pm 0.032$.

and 2.4 μm at a spectral resolution of 2500–2700 (Herter et al. 2008). In order to decrease the effect of bad pixels on the detector, we adopted the four-position ABCD nod pattern used by Muirhead et al. (2014) rather than the two-position ABBA pattern we used for our SpeX observations. With the exception of double star systems for which we altered the slit rotation to

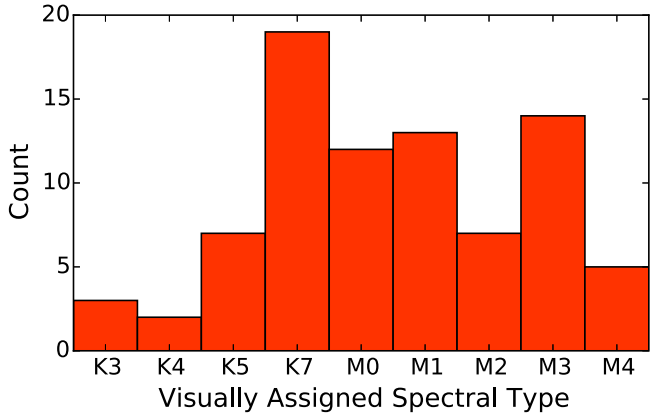

Figure 2. Distribution of visually assigned spectral types for the 74 stars in our cool dwarf sample.

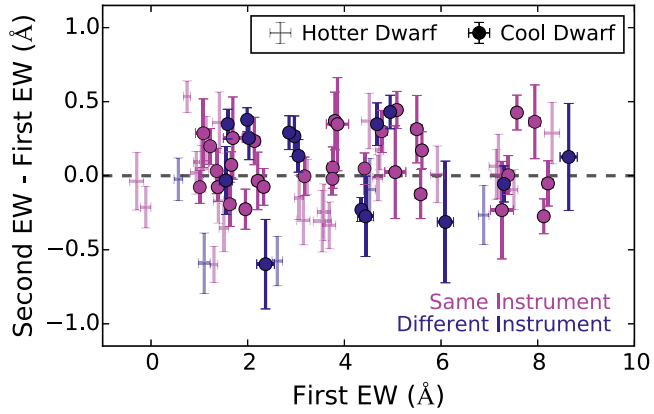

Figure 3. Repeatability of our equivalent width measurements when using the same instrument for both observations (magenta points) or different instruments for each observation (navy points). The 75 data points plotted here are the EW measured for five Mg and Al features in 30 spectra of 15 candidate low-mass dwarfs (two observations per star). Eight stars were later classified as cool dwarfs (large circles; spectral types K7, M0, and M1) and seven were classified as hotter dwarfs (small points). For reference, the gray dashed line marks zero difference between the two EW measurements.

place both stars in the slit when possible, we left the slit in a fixed east–west orientation. We calibrated our spectra using dome darks and dome flats acquired at both the beginning and end of the night.

3. Target Sample

The objective of our observing campaign was to determine the properties of K2 target stars and assess the planethood of associated planet candidates. Consequently, our targets were selected from lists of K2 planet candidates compiled by A. Vanderburg and the K2 California Consortium (K2C2). These early target lists are preliminary versions of planet candidate catalogs such as those published in Vanderburg et al. (2016) and Crossfield et al. (2016).

Of the 144 K2 targets observed, 99 (69%) appear in unpublished lists provided by A. Vanderburg, 28 (19%) were published in the Vanderburg et al. (2016) catalog, and 77 (53%) were reported in previously unpublished lists generated by K2C2. (These totals sum to >100% due to partial overlap between the Vanderburg and K2C2 candidate lists.) The K2C2

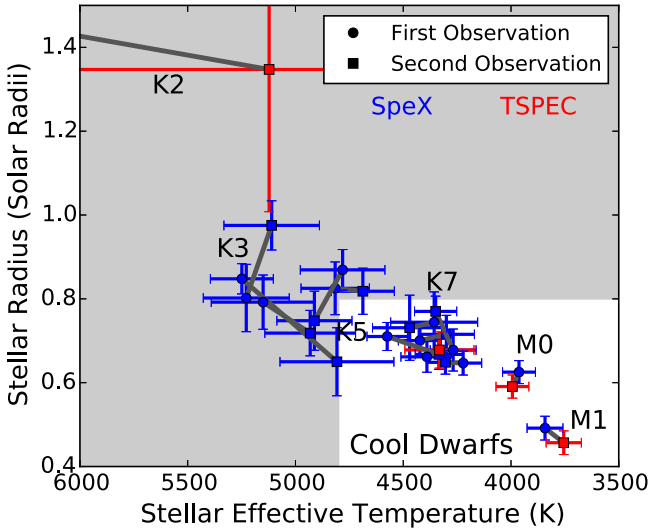

Figure 4. Repeatability of parameter estimates for the subsample of 15 stars with two observations. The data points mark the estimated temperatures and radii found by applying the Newton et al. (2015) EW relations to the first observations (circles) and second observations (squares) of each star. The colors differentiate between observations made using SpeX on the IRTF (blue) and TSPEC on the Palomar 200″ (red). The thick gray lines connect the two classifications for each star. The cluster of points near 4350 K and 0.7 $R_\odot$ contains five K7 dwarfs observed twice each. The white box indicates the boundaries of our cool dwarf sample: $T_{\rm eff} < 4800$ K, $R_\star < 0.8\,R_\odot$.

planet candidates from K2 Campaigns 0–4 were later published in Crossfield et al. (2016). Although we did not consult these catalogs for initial target selection, our target sample also contains 46 systems from Barros et al. (2016), 26 stars from Pope et al. (2016), 5 stars from Foreman-Mackey et al. (2015), 5 stars from Montet et al. (2015), and 4 stars from Adams et al. (2016).

The Vanderburg and K2C2 catalogs contain all of the planet candidates detected by the corresponding pipeline (`K2SFF` and `TERRA`, respectively) in the K2 light curves of stars proposed as individual GO targets. Neither pipeline considers stars observed as part of "super-stamps." Due to the heterogenous nature of the K2 target lists and the limited information provided in the EPIC during early K2 campaigns, the selected target sample is heavily biased. As noted by Huber et al. (2016), the K2 target lists are biased toward cool dwarfs. Overall, the set of stars observed during Campaigns 1–8 consisted primarily of K and M dwarfs (41%), F and G dwarfs (36%), and K giants (21%), but the giant fraction was higher for fields close to the galactic plane (see Table 2) than for fields at higher galactic latitude (Huber et al. 2016). Many GOs used a magnitude cut when proposing targets, which may have increased the representation of multiple star systems within the selected sample.

Due to the design of the K2 mission, our K2 targets were concentrated in distinct fields of the sky each spanning roughly 100 square degrees. We note the number of targets observed from each campaign in Table 2. As shown in Figure 1, the magnitude distribution of our K2 targets ranged from 6.2 to 13.1 in *Ks*, with a median *Ks* magnitude of 10.8. In the *Kepler* bandpass (similar to *V*-band), our targets had brightnesses of $Kp = 9.0$–16.3 and a median brightness of $Kp = 13.5$.

With each K2 data release, we initially prioritized observations of stars harboring small planet candidates

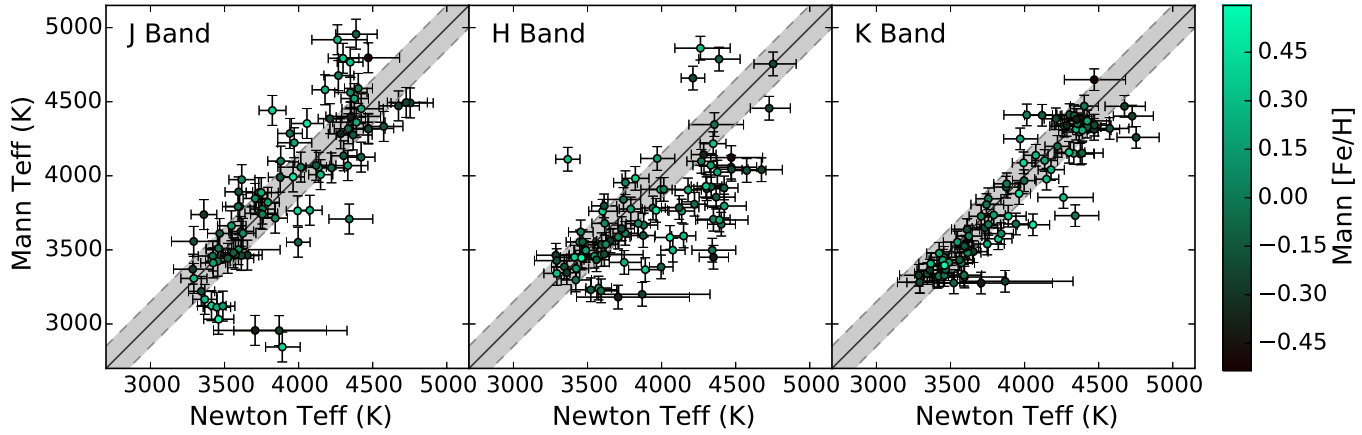

Figure 5. Comparison of temperatures derived using EW-based estimates from Newton et al. (2015) and spectral indices from Mann et al. (2013b) in *J* band (left), *H* band (middle), and *K* band (right). Points within the shaded region lie within 150 K of a one-to-one relation (solid line). All points are color-coded by [Fe/H], as indicated by the colorbar.

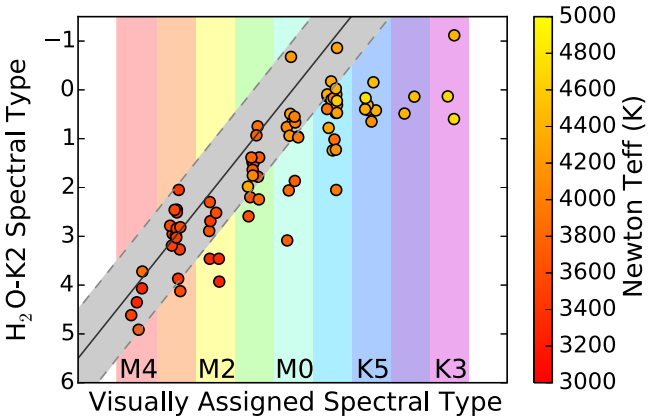

Figure 6. Numerical spectral types automatically derived from the H_2O-*K2* index vs. our visually determined spectral types. The points are color-coded based on the EW-based temperature estimate resulting from the Newton et al. (2015) relations. The gray shaded region denotes spectral types that fall within one spectral type of a one-to-one relation. For reference, the rainbow shading also denotes the spectral type ranges. We assigned visual spectral types at integer values, but the points are horizontally offset for clarity.

(estimated planet radius $<4\,R_\oplus$) and systems that could potentially be well-suited for high-precision radial velocity observations (host star brighter than $V = 12.5$ and estimated radial velocity semi-amplitude $K > 2\,\mathrm{m\,s^{-1}}$). Once we had exhausted those targets, we worked down the target list and observed increasingly fainter host stars harboring larger planets. Our goal was to select late K dwarfs and M dwarfs, but the initial stellar classifications were uncertain, particularly for the first K2 fields when the Huber et al. (2016) EPIC stellar catalog was not yet available. To ensure that few low-mass stars were excluded from our analysis, we adopted lenient criteria when selecting potential target stars. Our rough guidelines were $J - K > 0.5$ and, for stars with coarse initial temperature estimates, temperatures cooler than 4900 K. Concentrating on the brightest targets biased our sample toward giant stars and binary stars. Similarly, our selected $J - K$ color-cut also boosted the giant fraction by excluding hotter dwarfs with bluer $J - K$ colors without discarding giant stars with extremely red $J - K$ colors. The binary boost due to prioritizing bright targets may have been partially offset by our avoidance of stars with nearby companions detected in follow-up adaptive optics images.

4. Data Analysis and Stellar Characterization

We performed initial data reduction using the publicly available `Spextool` pipeline (Cushing et al. 2004) and a version customized for use with TripleSpec data (available upon request from M. Cushing). Both versions of the pipeline include the `xtellcor` telluric correction package (Vacca et al. 2003). As recommended in the `Spextool` manual, we selected the Paschen δ line at 1.005 μm when generating the convolution kernel used to apply the observed instrumental profile and rotational broadening to the Vega model spectrum.

4.1. Initial Classification

After completing the `Spextool` reduction, we used an interactive Python-based plotting interface to compare our spectra to the spectra of standard stars from the IRTF Spectral Library (Rayner et al. 2009). We allowed each model spectrum to shift slightly in wavelength space to accommodate differences in stellar radial velocities. Considering the *J*, *H*, and *K* bandpasses independently, we assessed the χ^2 of a fit of each model spectrum to our data and recorded the dwarf and giant models with the lowest χ^2.

We then considered the target spectrum holistically and assigned a single classification to the star. Although the focus of this analysis was to characterize planetary systems orbiting low-mass dwarfs, our target sample did include contamination from hotter and evolved stars. We list the 23 giants and 49 hotter dwarfs in Tables 3 and 4, respectively. We did not include either group in the more detailed analyses described in Section 4.2. For the purposes of identifying contamination, we rejected all stars that we visually classified as giants or dwarfs with spectral types earlier than K3. Table 4 also includes all stars for which the Newton et al. (2015) routines yielded estimated temperatures above 4800 K or radii larger than 0.8 $R_\odot$ (see Section 4.2). We display the reduced spectra for all targets in the Appendix. We have also posted our spectra and stellar classifications on the ExoFOP-K2 follow-up website.[11]

[11] https://exofop.ipac.caltech.edu/k2/

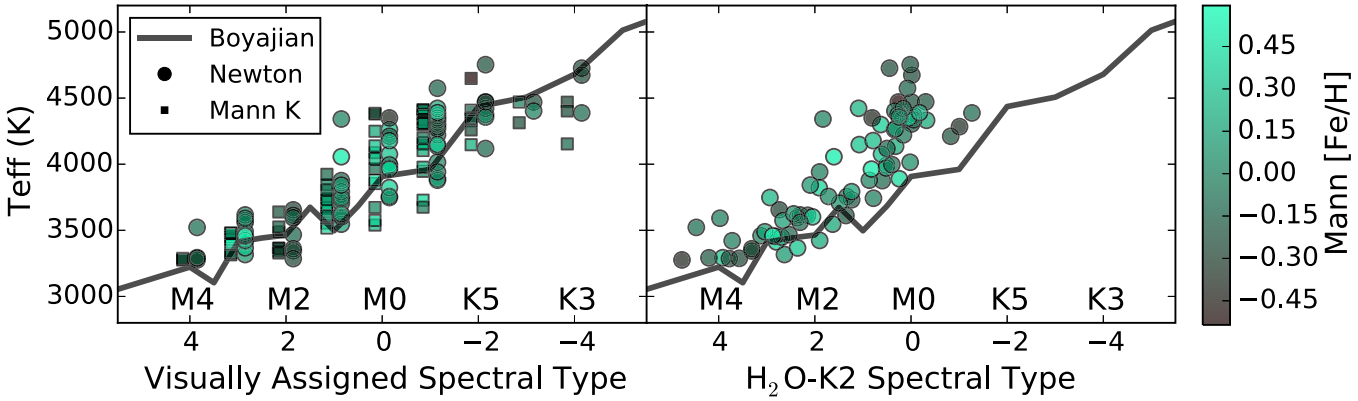

Figure 7. Temperatures from Newton et al. (2015) EW-based relation (circles) and Mann et al. (2013b) *K*-band relation (squares) vs. visually assigned spectral type (left) and automatically assigned H_2O-*K2* index-based spectral types (right). For reference, the black line shows the spectral types and temperatures reported by Boyajian et al. (2012) for interferometrically characterized stars. Note that Boyajian et al. (2012) report temperatures at half spectral types between M0 and M4. All points are color-coded by [Fe/H] as indicated by the colorbar.

Figure 2 displays the spectral type distribution of the stars in the selected cool dwarf sample. The sample includes stars with spectral types between K3 and M4, with a median spectral type of M0. These spectral types are rather coarse visual assignments (±1 subclass), so the spike at M3V may be a quirk of the particular template stars used for spectral type assignment rather than a true feature of the distribution. Due to the small sample size, the spike can also be explained by Poisson counting errors.

4.2. Detailed Stellar Characterization

For the stars that were visually identified as dwarfs with spectral types of K3 or later, we used a series of empirical relations to refine the stellar classification. We began by using the publicly available, IDL-based `tellrv`[12] and `nirew`[13] packages developed by Newton et al. (2014, 2015) to shift each spectrum to the stellar rest frame on an order-by-order basis, measure the equivalent widths of key spectral features, and estimate stellar properties. Specifically, the packages employ empirically based relations linking the equivalent widths of *H*-band Al and Mg features to stellar temperatures, radii, and luminosities (Newton et al. 2015). These relations are appropriate for stars with spectral types between mid-K and mid-M (i.e., temperatures of 3200–4800 K, radii of $0.18 < R_\star < 0.8 R_\odot$, and luminosities of $-2.5 < \log L/L_\odot < -0.5$). The relations were calibrated using IRTF/SpeX spectra (Newton et al. 2015) so we downgraded the Palomar/TSPEC spectra to match the lower resolution of IRTF/SpeX data before applying the relations. We note that neglecting the change in resolution can lead to systematic 0.1 Å differences in the measured EW due to variations in the amount of contamination included in the designated wavelength interval (Newton et al. 2015). As shown in Figure 3, we find generally consistent equivalent widths in spectra acquired on different occasions even if the two observations used separate instruments under variable observing conditions. Specifically, the median absolute difference in equivalent widths for the five cool dwarfs with repeated measurements using the same instrument was 0.2 Å (0.9σ). The median absolute difference for the three cool dwarfs with measurements from different instruments was 0.3 Å (1.9σ).

[12] https://github.com/ernewton/tellrv
[13] https://github.com/ernewton/nirew

In the original formulation of the `measure_hband` stellar characterization routine, the errors on stellar parameters are determined via a Monte Carlo simulation in which multiple realizations of noise are added to the spectra and the equivalent widths of features are re-measured. The errors are then determined by combining the random errors in the resulting EWs with the intrinsic scatter in the relations. This approach yields useful errors, but the adopted stellar parameters are taken from a single realization of the noise. For high SNR spectra, variations in the simulated noise might not lead to large changes in stellar properties, but for lower SNR spectra the estimated properties can differ considerably from one realization to the next. Several of our spectra have SNR of less than 200, which was the threshold used in the Newton et al. (2015) study. Accordingly, we altered `measure_hband` to calculate the temperatures, luminosities, and radii for each realization of the noise and report the 50th, 16th, and 84th percentiles as the best-fit values, lower error bars, and upper error bars, respectively.

Our changes significantly improve the reproducibility of temperature, luminosity, and radius estimates for stars with lower SNR spectra. For example, we repeated the classification of the M2 dwarf EPIC 206209135 five times using both the original and modified versions of `measure_hband`. For each classification, we determined parameter errors by generating 1000 noise realizations. The original code yielded estimated temperatures ranging from 3267 to 3461 K, radii of 0.32–0.35 $R_\odot$, and $-1.94 \leqslant \log L/L_{\odot\star} \leqslant -1.85$. The variations in the assigned temperatures and luminosities of 194 K and 0.09 $\log L_\odot$ were significantly larger than the individual error estimates of 85 K and 0.06 $\log L_\odot$ and the spread in assigned radii of 0.03 $R_\odot$ was equal to the individual radius errors. In comparison, our new method found $T_{\rm eff} = 3360 \pm 87$ K, $R_\star = 0.33 \pm 0.03\, R_\odot$, and $\log L_\star = -1.87 \pm 0.06 \log L_\odot$ in all cases. Due to the asymmetry of the resulting temperature and radius distributions for some stars, we also report separate upper and lower error bounds instead of forcing the errors to be symmetric in all cases. (EPIC 2106209135 is an example of a star with naturally symmetric errors.)

We confirmed that our cool dwarf classifications were repeatable by comparing our parameter estimates for the 15 stars observed on two different observing runs. Figure 4 reveals satisfactory agreement in the temperature and radius estimates for the eight stars cooler than 4800 K, the designated upper limit for our cool dwarf sample. Our results for the seven hotter

Table 5
Observation Dates, Spectral Types, and Radial Velocities for Stars Classified as Cool Dwarfs

EPIC	Campaign	Observation		Spectral Type[a]	H_2O-K2		RV[d] (km s^{-1})
		Date	Instru		Index[b]	SpType[c]	
201205469	1	2015 Jun 13	SpeX	K7V	1.03	0.39	−4.0
201208431	1	2015 May 05	SpeX	K7V	1.04	0.17	16.4
201345483	1	2015 May 05	SpeX	M0V	1.03	0.49	4.5
201549860	1	2015 Nov 26	SpeX	K4V	1.03	0.49	54.7
201617985	1	2015 Apr 16	SpeX	M1V	1.01	0.93	4.4
201635569	1	2015 May 05	SpeX	M0V	1.02	0.67	6.6
201637175	1	2015 May 05	SpeX	K7V	1.01	1.02	−8.4
201717274	1	2015 May 05	SpeX	M2V	0.89	3.93	43.1
201855371	1	2015 Apr 16	SpeX	K5V	1.02	0.65	−11.9
205924614	3	2015 Sep 24	SpeX	K7V	1.00	1.24	0.9
205924614	3	2015 Nov 26	SpeX	K7V	1.02	0.78	4.4
206011691	3	2015 Aug 07	SpeX	K7V	1.04	0.14	9.5
206011691	3	2015 Sep 24	SpeX	K7V	1.04	0.31	4.2
206119924	3	2015 Sep 24	SpeX	K7V	1.04	0.20	−16.8
206209135	3	2015 Sep 24	SpeX	M2V	0.91	3.46	−38.1
206312951	3	2015 Sep 24	SpeX	M1V	0.98	1.64	−14.0
206318379	3	2015 Sep 24	SpeX	M4V	0.88	4.07	11.7
210448987	4	2015 Nov 27	SpeX	K3V	1.04	0.13	−15.9
210489231	4	2015 Sep 24	SpeX	M1V	0.98	1.75	−56.6
210508766	4	2015 Sep 24	SpeX	M1V	1.02	0.75	−0.4
210558622	4	2015 Oct 14	SpeX	K7V	1.03	0.47	−0.1
210558622	4	2015 Nov 26	SpeX	K7V	1.03	0.36	−2.6
210564155	4	2015 Nov 27	SpeX	M2V	0.91	3.46	36.5
210707130	4	2015 Sep 24	SpeX	K5V	1.03	0.42	−2.4
210750726	4	2015 Sep 24	SpeX	M1V	0.94	2.59	2.5
210838726	4	2015 Sep 24	SpeX	M1V	0.99	1.39	18.6
210968143	4	2015 Sep 24	SpeX	K5V	1.04	0.31	20.9
211077024	4	2015 Nov 26	SpeX	M3V	0.92	3.19	23.2
211305568	5	2015 Nov 27	SpeX	M1V	0.99	1.50	29.7
211331236	5	2015 Nov 26	SpeX	M1V	0.99	1.48	2.0
211331236	5	2016 Apr 18	TSPEC	M1V	0.96	2.24	−5.3
211336288	5	2016 Mar 27	TSPEC	M0V	1.03	0.55	19.4
211357309	5	2015 Nov 27	SpeX	M1V	0.99	1.38	18.5
211428897[e]	5	2015 Nov 26	SpeX	M2V	0.95	2.52	25.6
211509553	5	2016 Mar 27	TSPEC	M0V	0.97	1.87	−14.7
211680698	5	2016 Mar 28	TSPEC	K3V	1.02	0.60	−29.4
211694226A	5	2016 Mar 8	SpeX	M3V	0.93	2.98	21.2
211694226B	5	2016 Mar 8	SpeX	M3V	0.93	2.84	24.0
211762841	5	2016 Mar 4	SpeX	K7V	1.03	0.47	24.6
211770795	5	2016 Apr 18	TSPEC	K5V	1.04	0.17	−44.3
211791178	5	2016 Mar 27	TSPEC	M0V	1.01	0.96	61.5
211799258	5	2016 Mar 8	SpeX	M3V	0.93	2.78	44.6
211817229	5	2016 Mar 4	SpeX	M4V	0.85	4.91	28.2
211818569	5	2016 Feb 19	TSPEC	K5V	1.06	−0.16	24.9
211822797	5	2016 Mar 27	TSPEC	K7V	1.00	1.23	28.3
211826814	5	2016 Feb 19	TSPEC	M4V	0.90	3.72	24.1
211831378	5	2016 Apr 18	TSPEC	M0V	0.92	3.08	3.7
211839798	5	2016 Mar 4	SpeX	M4V	0.86	4.62	30.5
211924657	5	2016 Mar 8	SpeX	M3V	0.89	3.87	40.0
211965883	5	2016 Mar 27	TSPEC	M0V	1.08	−0.68	37.3
211969807	5	2016 Mar 8	SpeX	M1V	0.98	1.78	33.5
211970234	5	2016 Apr 18	TSPEC	M4V	0.87	4.35	−8.5
211988320	5	2016 Mar 27	TSPEC	K7V	1.09	−0.86	79.1
212006344	5	2015 Nov 26	SpeX	M0V	1.02	0.65	−13.3
212006344	5	2016 Feb 19	TSPEC	M0V	1.01	0.97	−15.5
212069861	5	2015 Nov 26	SpeX	M0V	1.02	0.76	25.3
212154564	5	2016 Mar 27	TSPEC	M3V	0.95	2.46	20.9
212354731	6	2016 Mar 28	TSPEC	M3V	0.88	4.12	−24.4
212398486	6	2016 Mar 4	SpeX	M2V	0.93	2.89	−19.0
212443973	6	2016 Mar 27	TSPEC	M3V	0.96	2.05	0.7
212460519	6	2016 Mar 8	SpeX	K7V	1.05	0.09	−1.6
212554013	6	2016 Apr 18	TSPEC	K3V	1.10	−1.12	−60.0

Table 5
(Continued)

EPIC	Campaign	Observation		Spectral Type[a]	H_2O-K2		RV[d] (km s^{-1})
		Date	Instru		Index[b]	SpType[c]	
212565386	6	2016 Mar 10	SpeX	M1V	0.97	1.98	−38.7
212572452	6	2016 Mar 10	SpeX	K7V	1.06	−0.17	5.7
212572452	6	2016 Mar 27	TSPEC	K7V	1.05	−0.03	6.0
212628098	6	2016 Apr 18	TSPEC	K7V	0.96	2.05	−2.2
212634172	6	2016 Mar 4	SpeX	M3V	0.93	2.95	23.2
212679181	6	2016 Mar 4	SpeX	M3V	0.95	2.45	13.3
212679798	6	2016 Apr 18	TSPEC	M0V	0.96	2.06	4.0
212686205	6	2016 Mar 8	SpeX	K4V	1.04	0.14	−9.6
212690867	6	2016 Mar 8	SpeX	M2V	0.95	2.30	6.5
212773272	6	2016 Apr 18	TSPEC	M3V	0.95	2.51	−7.2
212773309	6	2016 Mar 28	TSPEC	M0V	1.01	0.94	−13.6
212773309B	6	2016 Mar 28	TSPEC	M3V	0.92	3.03	−4.1
213951550	7	2016 May 6	SpeX	M3V	0.93	2.81	−77.2
214254518	7	2016 May 5	SpeX	K7V	1.05	0.09	17.6
214254518	7	2016 Oct 26	SpeX	K7V	1.04	0.22	17.3
214522613	7	2016 May 5	SpeX	M1V	0.96	2.20	35.9
214787262	7	2016 May 5	SpeX	M3V	0.91	3.27	−24.1
216892056	7	2016 May 5	SpeX	M2V	0.94	2.69	−82.8
217941732	7	2016 May 5	SpeX	K5V	1.03	0.41	−49.8
217941732	7	2016 Oct 26	SpeX	K5V	1.03	0.40	−50.9

Notes.
[a] Spectral types are coarse assignments based on visual inspection of the near-infrared spectra collected in this paper. The assigned spectral types have errors of roughly ±1 subtype. (See Section 4.1 for details.)
[b] H_2O-*K2* index (Rojas-Ayala et al. 2012). Although we report H_2O-*K2* indices and index-based spectral types for the full cool dwarf sample, these values are meaningless for the hotter stars.
[c] Spectral type estimated using the H_2O-*K2*—spectral type relation introduced by Newton et al. (2014). On this scale, a spectral type of 0 corresponds to MV0 and positive values indicate correspondingly later M dwarf spectral types (e.g., 2 = M2V). Negative values indicate K subtypes (i.e., −1 = K7V, −2 = K5V).
[d] Reported absolute radial velocities are the median of the values estimated by cross-correlating the telluric lines in our *J*-, *H*-, and *K*-band spectra with a theoretical atmospheric transmission spectrum using the `tellrv` framework developed by Newton et al. (2014).
[e] Keck AO imaging by D. Ciardi and Gemini speckle imaging by M. Everett revealed that the star is actually a visual binary with a separation of roughly 1.″1(https://exofop.ipac.caltech.edu/k2/edit_target.php?id=211428897).

stars are less consistent, but the relations from Newton et al. (2015) are not valid at those temperatures.

4.2.1. Stellar Effective Temperature

For comparison, we also determined stellar effective temperatures using the *J*-, *H*-, and *K*-band temperature-sensitive indices and relations presented by Mann et al. (2013b). We then applied the temperature–metallicity–radius relation from Mann et al. (2015) to assign stellar radii. Next, we determined luminosities and masses from the estimated stellar effective temperatures using relations 7 and 8 from Mann et al. (2013b). These relations are based on stars with effective temperatures between 3238 and 4777 K and radii between 0.19 and 0.78 $R_\odot$.

In Figure 5, we plot the temperature estimates generated using the Newton et al. (2015) pipeline against those from the Mann et al. (2013b) relations. The Mann *H*-band-based temperatures display considerable scatter and are systematically lower than the three other estimates (the temperatures based on the Newton et al. (2015) routines, the *J*-band temperatures, and the *K*-band temperatures). This discrepancy, which is most noticeable for stars hotter than 4000 K, is likely caused by saturation of the index as the continuum flattens for hotter stars. The *J*-band temperatures also display large scatter, but they are more centered along a one-to-one relation than the *H*-band estimates. Due to the much tighter correlation observed between the *K*-band temperatures and the EW-based temperature estimates, we adopt the *K*-band temperatures as the "Mann temperatures" for our stars. We also see discrepancies for stars with $T_{\rm eff} < 3500$. There are three stars for which the temperature inferred using the Newton et al. (2015) relations is larger than that inferred from the *J*-, *H*-, and *K*-band temperatures, The error bars in the temperature inferred from the Newton et al. (2015) relations are also large. This is caused by the disappearance of the Mg and Al features in the coolest dwarf stars, which tends to result in an overestimate of $T_{\rm eff}$. Al is weaker at lower metallicity, consistent with this effect only being seen in metal-poor stars at the limits of the calibration.

Newton et al. (2015) also compared temperature estimates derived using their empirical relations with those based on the Mann et al. (2013b) temperature-sensitive indices. They found large standard deviations of $\sigma_{\Delta T} = 140$ K and $\sigma_{\Delta T} = 170$ K in *J* band and *H* band, respectively, between temperatures determined using each method, which they attributed to telluric contamination. In contrast, the standard deviation between the Newton et al. (2015) estimates and the Mann et al. (2013b) *K*-band estimates was only $\sigma_{\Delta T} = 90$ K, suggesting that the *K*-band relation is less contaminated by telluric features.

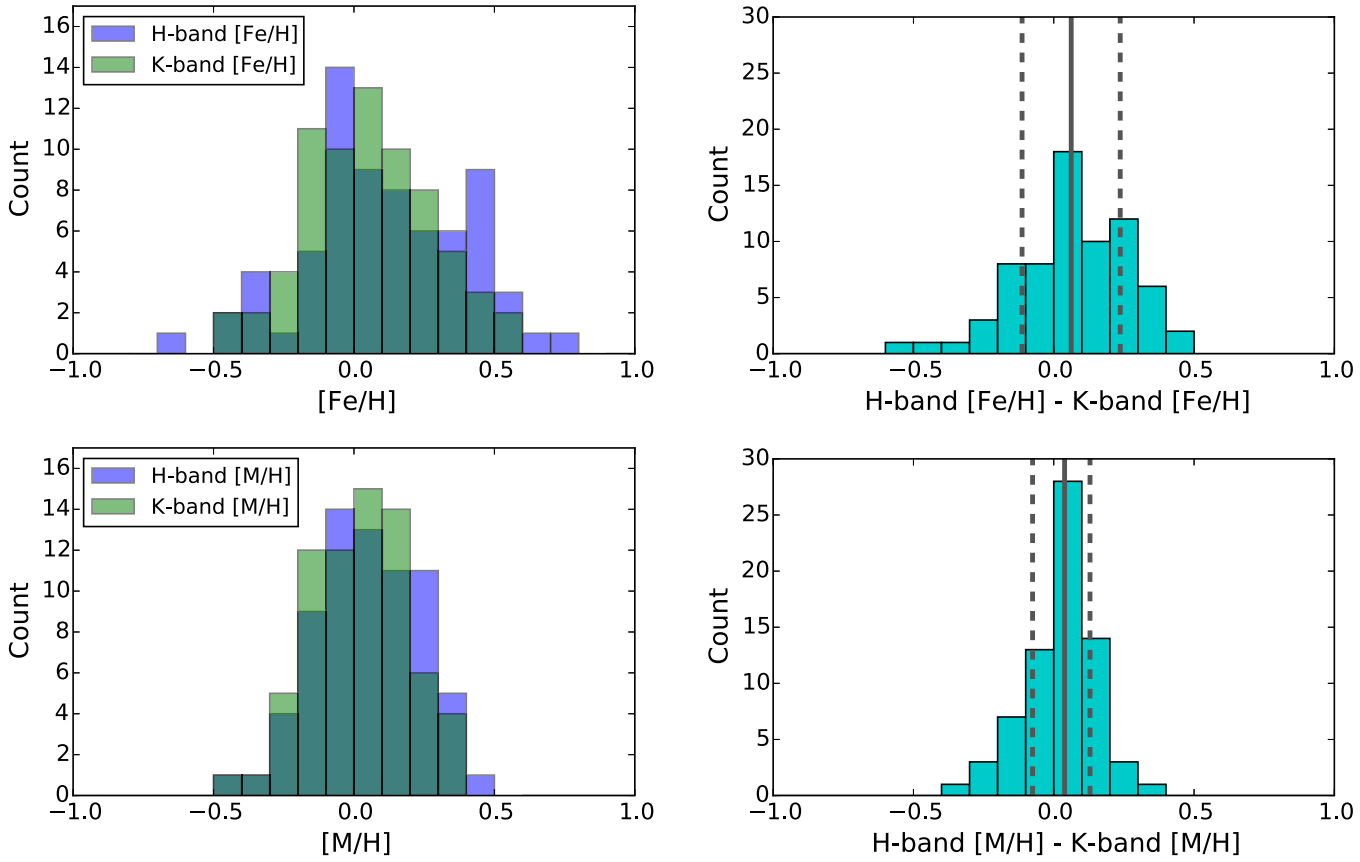

Figure 8. Estimated metallicities for the 63 cool dwarfs with spectral types of K7 or later. The top two panels display the distribution of [Fe/H] (left) and [M/H] (right) calculated using separate relations from Mann et al. (2013a) for *H*-band (blue) and *K*-band (green) spectra. The bottom two panels display the distributions of differences in the *H*-band and *K*-band estimates of [M/H] (left) and [Fe/H] (right). The green lines indicate the median values (solid lines) and the 16th and 84th percentile values (dashed lines).

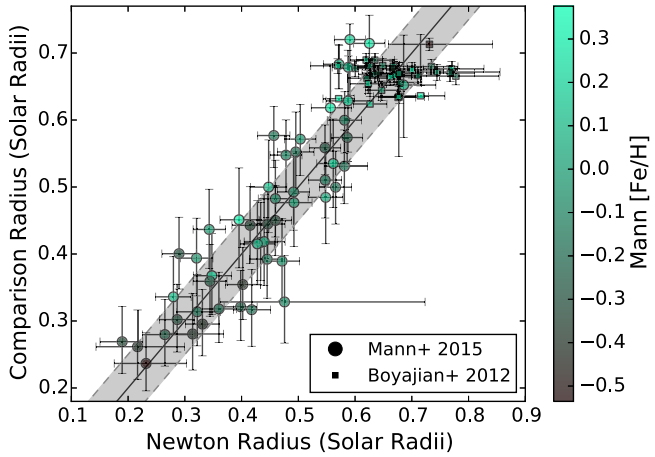

Figure 9. Comparison of radii derived directly using the Newton et al. (2015) relations and indirectly via the Mann et al. (2015, circles) temperature–metallicity–radius relation or Boyajian et al. (2012, squares) temperature–radius relation. Points within the shaded region lie within 0.05 $R_{\odot}$ of a one-to-one relation (solid line). The data points are color-coded by [M/H] as measured using relations from Mann et al. (2013a).

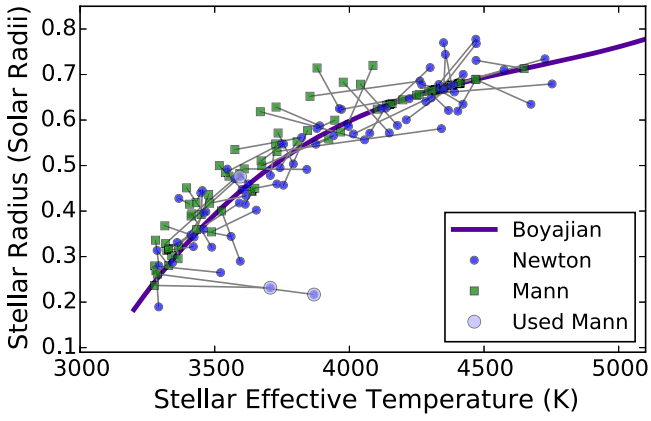

Figure 10. Comparison of temperatures and radii derived using relations from Newton et al. (2015) and Mann et al. (2015). The gray lines connect the values from the Newton relations (blue circles) and Mann relation (green squares) for each star. The three mid-M dwarfs highlighted with light blue circles have Al-a EW below the calibration range for the Newton temperature relations. For those three stars only, we adopt the Mann parameters instead. For reference, the purple line displays the third-order temperature–radius polynomial presented in Equation (8) of Boyajian et al. (2012).

For our sample of stars, the agreement between the two methods is much worse: we measure standard deviations of 278, 311, and 162 K for the temperature differences between the EW-based estimates and the estimates based on the *J*-band, *H*-band, and *K*-band spectral indices, respectively. The median temperature differences are 13, 143, and 64 K for *J* band, *H* band, and *K* band, respectively, with the EW-based estimates higher than the spectral index-based estimate for

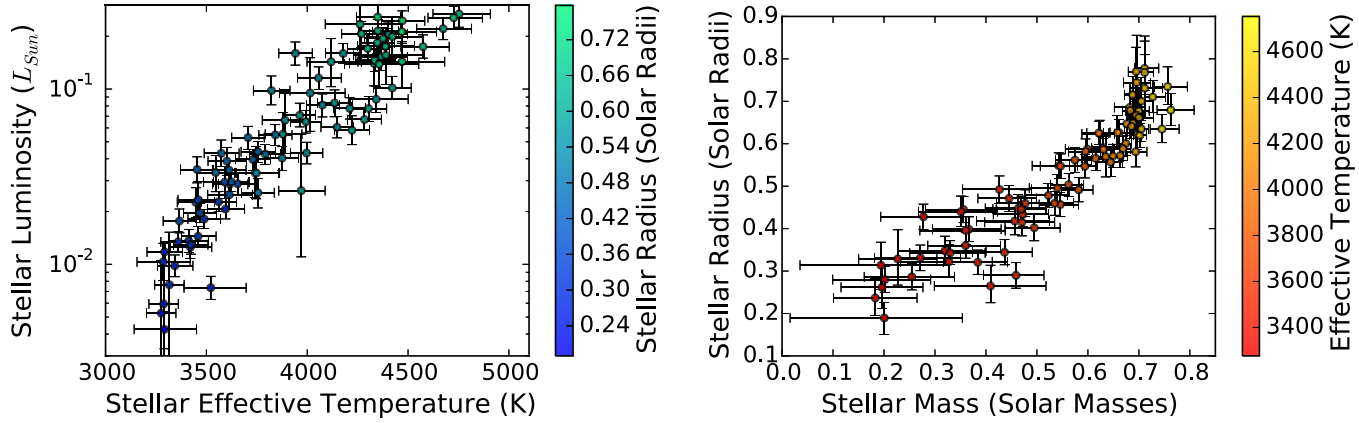

Figure 11. Revised parameters for the cool dwarf sample. Left: revised stellar luminosity vs. stellar effective temperature with points shaded according to revised stellar radii. Right: revised radii and masses with points shaded according to revised stellar effective temperatures.

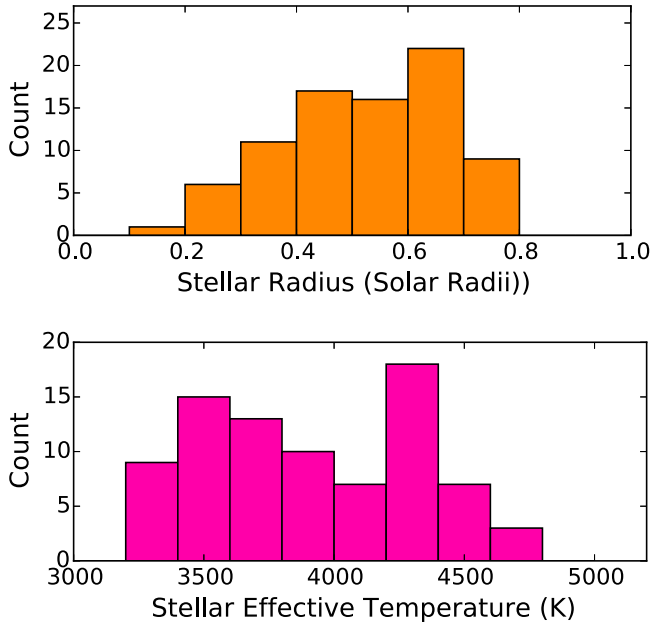

Figure 12. Distribution of radii (top) and effective temperatures (bottom) for the stars in our cool dwarf sample.

H and *K* bands and lower for *J* band. The significantly poorer agreement is likely due to the differences between the Newton et al. (2015) stellar sample and our stellar sample. The Newton et al. (2015) sample was dominated by mid- and late-M dwarfs with effective temperatures between 3000 and 3500 K. In contrast, our targets are primarily late K dwarfs and early M dwarfs.

For an additional check of our stellar classifications, we applied the H_2O-K2 index–spectral type relation calibrated by Newton et al. (2014) to estimate near-infrared spectral types. The H_2O-K2 index (Rojas-Ayala et al. 2012) provides an estimate of the level of water absorption in an M dwarf spectrum by measuring the shape of the spectrum between 2.07 and 2.38 μm. Higher values indicate lower H_2O opacity and therefore hotter temperatures. The H_2O-K2 index is the second-generation version of the H_2O-K index introduced by Covey et al. (2010) and uses slightly different portions of the spectrum to avoid contamination from atomic lines in early M dwarfs. The index is gravity-insensitive for stars with effective temperatures between 3000 and 3800 K and metallicity-insensitive for stars cooler than 4000 K. The H_2O-K2 index saturates near 4000 K, so these index measurements and spectral types are not valid for the hotter stars in our sample.

As shown in Figure 6, our visually assigned spectral types and the index-based spectral types agree well for stars cooler than roughly 3800 K. Above this temperature, the index-based spectral types plateau near M1 due to the inapplicability of the index for the earliest M dwarfs. The saturation of the H_2O-K2 index is highlighted in Figure 7, which provides an alternative comparison of our spectral type assignments and temperature estimates. In the left panel, we show that our visually assigned spectral types display the expected correlation with temperature throughout the spectral type range of our sample. In contrast, the index-based spectral types deviate from the expected correlation for stars earlier than M1V. We list the visually assigned and index-based spectral types for the cool dwarf sample in Table 5.

4.2.2. Stellar Metallicities

We estimated [Fe/H] and [M/H] using the relations from Mann et al. (2013a). The latest stars in our sample are M4 dwarfs, so we did not need to transition from the metallicity relations for K7−M5 dwarfs provided by Mann et al. (2013a) to the relations for M4.5–M9.5 dwarfs from Mann et al. (2014). We calculated metallicities using *H*-band and *K*-band spectra separately and compare the resulting distributions of [Fe/H] and [M/H] in Figure 8. On average, a typical star in our cool dwarf sample has near-solar metallicity. Averaging the *H*-band and *K*-band estimates for each star, we obtain median metallicities of [Fe/H] = 0.02 and [M/H] = 0.00. Figure 8 also displays distributions of the differences between the *H*-band and *K*-band metallicity estimates; they agree at the 1σ level. Although our cool dwarf sample includes 11 mid-K dwarfs, we restricted our metallicity analysis to the 63 cool dwarfs with spectral types of K7 or later.

4.2.3. Stellar Radii

We infer stellar radius using the methods from Newton et al. (2015) and Mann et al. (2015). The former are derived directly

Table 6
Inferred Stellar Parameters for Low-mass Dwarfs

			Teff (K)			Radius ($R_\odot$)			Mass ($M_\odot$)			Luminosity ($\log L_*/L_\odot$)		
EPIC	Date	SpType[a]	Val	−Err	+Err	Val	−Err	+Err	Val	−Err	+Err	Val	−Err	+Err
201205469	2015 Jun 13	K7V	3890	121	113	0.587	0.039	0.039	0.599	0.043	0.035	−1.178	0.188	0.175
201208431	2015 May 05	K7V	4015	173	155	0.569	0.047	0.049	0.635	0.046	0.035	−1.023	0.219	0.202
201345483	2015 May 05	M0V	4262	201	173	0.686	0.045	0.057	0.682	0.030	0.028	−0.630	0.218	0.198
201549860	2015 Nov 26	K4V	4403	96	93	0.620	0.028	0.029	0.702	0.013	0.013	−0.688	0.073	0.071
201617985	2015 Apr 16	M1V	3742	116	105	0.496	0.032	0.032	0.540	0.055	0.048	−1.480	0.141	0.134
201635569	2015 May 05	M0V	3970	118	112	0.623	0.032	0.032	0.623	0.035	0.028	−1.580	0.378	0.321
201637175	2015 May 05	K7V	3879	95	87	0.582	0.031	0.030	0.595	0.033	0.029	−1.258	0.135	0.124
201717274	2015 May 05	M2V	3286	134	130	0.314	0.057	0.054	0.194	0.159	0.133	−1.986	0.106	0.106
201855371	2015 Apr 16	K5V	4118	133	119	0.626	0.036	0.041	0.658	0.027	0.023	−0.845	0.142	0.133
205924614	2015 Sep 24	K7V	4423	149	130	0.700	0.045	0.056	0.705	0.018	0.022	−0.701	0.125	0.116
205924614[b]	2015 Nov 26	K7V	4300	107	100	0.715	0.040	0.043	0.688	0.015	0.015	−0.769	0.079	0.081
206011691	2015 Aug 07	K7V	4304	90	86	0.649	0.029	0.029	0.688	0.013	0.012	−1.111	0.072	0.071
206011691[b]	2015 Sep 24	K7V	4222	88	84	0.647	0.028	0.029	0.676	0.015	0.013	−1.235	0.082	0.083
206119924	2015 Sep 24	K7V	4348	86	88	0.669	0.030	0.030	0.695	0.013	0.012	−0.736	0.063	0.063
206209135	2015 Sep 24	M2V	3360	87	86	0.331	0.030	0.030	0.271	0.091	0.079	−1.872	0.059	0.058
206312951	2015 Sep 24	M1V	3707	80	81	0.478	0.028	0.028	0.523	0.045	0.037	−1.277	0.066	0.064
206318379	2015 Sep 24	M4V	3293	89	87	0.280	0.031	0.031	0.201	0.102	0.090	−1.929	0.059	0.061
210448987	2015 Nov 27	K3V	4674	141	131	0.635	0.032	0.035	0.745	0.023	0.034	−0.656	0.062	0.059
210489231	2015 Sep 24	M1V	4056	113	104	0.557	0.034	0.037	0.645	0.027	0.022	−0.937	0.067	0.063
210508766	2015 Sep 24	M1V	3876	81	80	0.547	0.028	0.028	0.594	0.031	0.025	−1.393	0.071	0.066
210558622[b]	2015 Oct 14	K7V	4268	105	98	0.678	0.036	0.040	0.683	0.016	0.015	−0.685	0.076	0.070
210558622	2015 Nov 26	K7V	4350	112	106	0.770	0.050	0.057	0.695	0.015	0.016	−0.590	0.076	0.070
210564155	2015 Nov 27	M2V	3344	90	87	0.286	0.031	0.030	0.255	0.093	0.084	−2.008	0.062	0.061
210707130	2015 Sep 24	K5V	4376	95	90	0.676	0.031	0.031	0.698	0.013	0.013	−0.711	0.063	0.062
210750726	2015 Sep 24	M1V	3624	88	87	0.460	0.030	0.032	0.477	0.057	0.048	−1.530	0.055	0.054
210838726	2015 Sep 24	M1V	3792	78	78	0.503	0.028	0.028	0.562	0.036	0.030	−1.371	0.058	0.057
210968143	2015 Sep 24	K5V	4422	93	91	0.635	0.029	0.029	0.705	0.013	0.013	−0.994	0.064	0.066
211077024	2015 Nov 26	M3V	3489	81	80	0.321	0.029	0.029	0.384	0.067	0.058	−1.742	0.054	0.054
211305568	2015 Nov 27	M1V	3612	85	84	0.446	0.030	0.031	0.470	0.056	0.048	−1.462	0.057	0.056
211331236	2015 Nov 26	M1V	3755	85	83	0.457	0.028	0.028	0.546	0.042	0.035	−1.358	0.061	0.059
211331236[b]	2016 Apr 18	M1V	3842	82	82	0.492	0.028	0.028	0.582	0.034	0.028	−1.262	0.060	0.060
211336288	2016 Mar 27	M0V	3997	80	79	0.586	0.027	0.027	0.630	0.022	0.019	−1.365	0.062	0.061
211357309	2015 Nov 27	M1V	3731	86	85	0.460	0.028	0.028	0.535	0.045	0.038	−1.402	0.060	0.059
211428897	2015 Nov 26	M2V	3595	95	91	0.290	0.030	0.030	0.459	0.064	0.055	−1.685	0.056	0.058
211509553	2016 Mar 27	M0V	3756	81	80	0.547	0.029	0.029	0.546	0.040	0.034	−1.592	0.087	0.081
211680698	2016 Mar 28	K3V	4726	143	127	0.735	0.043	0.047	0.756	0.025	0.039	−0.593	0.063	0.061
211694226a	2016 Mar 8	M3V	3454	83	82	0.445	0.031	0.031	0.356	0.074	0.064	−1.459	0.076	0.073
211694226b	2016 Mar 8	M3V	3448	93	92	0.440	0.035	0.037	0.351	0.084	0.072	−1.647	0.086	0.084
211762841	2016 Mar 4	K7V	4136	87	86	0.626	0.029	0.030	0.661	0.018	0.015	−1.080	0.078	0.075
211770795	2016 Apr 18	K5V	4753	155	129	0.679	0.036	0.038	0.763	0.027	0.046	−0.572	0.076	0.070
211791178	2016 Mar 27	M0V	4350	102	96	0.667	0.034	0.038	0.695	0.014	0.014	−0.669	0.068	0.068
211799258[c]	2016 Mar 8	M3V	3317	73	73	0.328	0.062	0.069	0.227	0.077	0.077	−2.117	0.373129	0.373129
211817229[c]	2016 Mar 4	M4V	3276	73	73	0.237	0.041	0.046	0.183	0.082	0.082	−2.279	0.676023	0.676023
211818569	2016 Feb 19	K5V	4471	112	104	0.768	0.042	0.042	0.712	0.014	0.017	−0.611	0.058	0.057
211822797	2016 Mar 27	K7V	4148	82	80	0.572	0.027	0.027	0.663	0.016	0.014	−1.218	0.061	0.061
211826814[c]	2016 Feb 19	M4V	3288	73	73	0.262	0.049	0.055	0.196	0.080	0.080	−2.226	0.539306	0.539306
211831378	2016 Apr 18	M0V	3748	115	101	0.548	0.031	0.031	0.543	0.052	0.047	−1.480	0.148	0.154
211839798	2016 Mar 4	M4V	3522	175	133	0.265	0.039	0.049	0.409	0.110	0.109	−2.134	0.067	0.065
211924657	2016 Mar 8	M3V	3421	106	98	0.322	0.036	0.041	0.327	0.095	0.085	−1.902	0.064	0.063
211965883	2016 Mar 27	M0V	4211	80	79	0.600	0.027	0.027	0.674	0.014	0.012	−1.110	0.061	0.060
211969807	2016 Mar 8	M1V	3546	99	95	0.492	0.032	0.032	0.427	0.072	0.063	−1.476	0.109	0.100
211970234	2016 Apr 18	M4V	3292	159	150	0.190	0.039	0.036	0.200	0.185	0.153	−2.371	0.111	0.101
211988320	2016 Mar 27	K7V	4284	84	84	0.641	0.028	0.029	0.685	0.013	0.012	−1.174	0.059	0.058
212006344[b]	2015 Nov 26	M0V	3993	78	76	0.591	0.027	0.027	0.630	0.022	0.018	−1.186	0.065	0.066
212006344	2016 Feb 19	M0V	3963	77	76	0.625	0.028	0.028	0.621	0.024	0.020	−1.150	0.066	0.069
212069861	2015 Nov 26	M0V	4076	83	81	0.571	0.028	0.028	0.649	0.019	0.016	−1.091	0.068	0.063
212154564	2016 Mar 27	M3V	3561	87	84	0.344	0.030	0.030	0.436	0.062	0.054	−1.643	0.058	0.058
212354731	2016 Mar 28	M3V	3591	119	106	0.418	0.032	0.033	0.457	0.075	0.068	−1.531	0.096	0.091
212398486	2016 Mar 4	M2V	3654	100	92	0.402	0.031	0.031	0.495	0.057	0.051	−1.540	0.067	0.064
212443973	2016 Mar 27	M3V	3423	84	84	0.343	0.028	0.028	0.330	0.079	0.069	−1.888	0.054	0.054
212460519	2016 Mar 8	K7V	4368	128	115	0.621	0.034	0.036	0.697	0.016	0.018	−0.816	0.080	0.075
212554013	2016 Apr 18	K3V	4388	142	137	0.677	0.045	0.052	0.700	0.019	0.020	−0.757	0.080	0.078
212565386	2016 Mar 10	M1V	4342	159	137	0.581	0.036	0.041	0.694	0.020	0.022	−1.058	0.075	0.074

Table 6
(Continued)

EPIC	Date	SpType[a]	Teff (K)			Radius ($R_\odot$)			Mass ($M_\odot$)			Luminosity ($\log L_*/L_\odot$)		
			Val	−Err	+Err	Val	−Err	+Err	Val	−Err	+Err	Val	−Err	+Err
212572452	2016 Mar 27	K7V	4390	193	160	0.662	0.043	0.053	0.700	0.023	0.028	−0.807	0.165	0.155
212572452[b]	2016 Mar 10	K7V	4332	135	121	0.678	0.037	0.044	0.692	0.018	0.019	−0.854	0.128	0.120
212628098	2016 Apr 18	K7V	3942	84	82	0.566	0.028	0.028	0.615	0.027	0.022	−0.796	0.067	0.065
212634172	2016 Mar 4	M3V	3412	98	94	0.348	0.033	0.034	0.320	0.092	0.081	−1.866	0.064	0.062
212679181	2016 Mar 4	M3V	3616	89	87	0.434	0.029	0.029	0.472	0.058	0.050	−1.544	0.056	0.058
212679798	2016 Apr 18	M0V	3823	92	89	0.562	0.029	0.029	0.575	0.039	0.032	−1.009	0.081	0.084
212686205	2016 Mar 8	K4V	4470	172	145	0.778	0.061	0.076	0.711	0.020	0.028	−0.673	0.066	0.065
212690867	2016 Mar 8	M2V	3614	118	107	0.415	0.032	0.033	0.471	0.073	0.064	−1.603	0.078	0.077
212773272	2016 Apr 18	M3V	3367	82	81	0.428	0.030	0.030	0.277	0.084	0.074	−1.753	0.067	0.069
212773309	2016 Mar 28	M0V	4178	90	87	0.588	0.029	0.029	0.669	0.016	0.014	−0.797	0.056	0.057
212773309B	2016 Mar 28	M3V	3459	103	100	0.396	0.034	0.034	0.360	0.090	0.078	−1.632	0.097	0.104
213951550	2016 May 6	M3V	3574	88	85	0.471	0.030	0.030	0.445	0.061	0.054	−1.367	0.075	0.076
214254518[b]	2016 May 5	K7V	4335	102	94	0.668	0.033	0.037	0.693	0.014	0.014	−0.836	0.066	0.066
214254518	2016 Oct 26	K7V	4574	130	110	0.710	0.036	0.038	0.727	0.017	0.024	−0.758	0.065	0.067
214522613	2016 May 5	M1V	3602	99	94	0.448	0.032	0.032	0.463	0.065	0.056	−1.412	0.084	0.080
214787262	2016 May 5	M3V	3459	89	84	0.360	0.030	0.031	0.360	0.074	0.068	−1.841	0.056	0.055
216892056	2016 May 5	M2V	3467	84	82	0.398	0.029	0.029	0.367	0.071	0.063	−1.707	0.057	0.056
217941732	2016 May 5	K5V	4470	211	202	0.731	0.072	0.111	0.711	0.028	0.035	−0.844	0.153	0.116
217941732[b]	2016 Oct 26	K5V	4356	197	172	0.744	0.078	0.111	0.696	0.026	0.028	−0.858	0.132	0.126

Notes.
[a] Spectral types are coarse assignments based on visual inspection of the near-infrared spectra collected in this paper. The assigned spectral types have errors of roughly ±1 subtype. (See Section 4.1 for details.)
[b] Star observed twice to check the repeatability of our analysis. These are the higher precision estimates.
[c] The Al-a EW for these stars are below the calibration range for the Newton et al. (2015) relations. Adopted parameters are based on the Mann et al. (2013a, 2013b, 2015) relations.

from the EWs. The latter use $T_{\rm eff}$ and metallicity to estimate radii indirectly; for $T_{\rm eff}$, we use the K-band temperatures (which we refer to as "Mann temperatures," see Section 4.2.1). The Mann et al. (2015) temperature–metallicity–radius relation is valid for stars with temperatures between 2700 and 4100 K, but many of the stars in our sample are hotter than this upper limit. For the stars for which the Mann et al. (2015) relations yield temperatures hotter than 4100 K, we instead compare the Newton et al. (2015) radii to the radii estimated by applying the temperature–radius relation provided in Equation (8) of Boyajian et al. (2012) using the Mann temperatures.

We display the resulting radius estimates in Figure 9. The Mann et al. (2015) methodology and the Newton et al. (2015) routines yield similar radii: the median radius difference is 0.01 $R_\odot$ (the Mann radii are larger) and the standard deviation of the differences is 0.06 $R_\odot$. For comparison, the median reported radius errors are 0.03 $R_\odot$ for the Newton et al. (2015) values and 0.05 $R_\odot$ for the Mann et al. (2015) values. Looking at the hotter stars, the median difference between the Newton radii and Boyajian et al. (2012) radii is only 0.002 $R_\odot$ and the standard deviation of the difference is 0.05 $R_\odot$

As shown in Figure 10, the primary reason why the temperature agreement looks worse for the coolest stars is because three cool stars (EPIC 211817229, EPIC 211799258, and EPIC 211826814) have significantly different parameters using the two methods. Based on the sample of stars with interferometrically constrained properties, the expected temperatures and radii of M5.5–M3 dwarfs are 3054–3412 K and 0.14–0.41 $R_\odot$, respectively (Boyajian et al. 2012). Although these stars were visually classified as M3 or M4 dwarfs, the Newton et al. (2015) routines assigned them high temperatures of 3594–3869 K because the Al-a EW measured in their spectra were below the lower limit of the calibration sample (see Table 7 for EW measurements). The Mann routines assigned the stars cooler temperatures of 3276–3317 K. Due to the better agreement between the Mann temperatures and expected temperatures of mid-M dwarfs, we chose to adopt the Mann et al. classifications for those three stars.

4.2.4. Stellar Luminosities

We compared the stellar luminosities estimated using the EW-based relation from Newton et al. (2015) to those found using the temperature–luminosity relation from Mann et al. (2013b). Due to the functional nature of the Mann et al. (2013b) relation, the Mann values followed a single track whereas the Newton values displayed scatter about that relation. Ignoring the three mid-M dwarfs that are too cool for the Newton relations, the luminosity differences (Newton–Mann) have a median value of 0.008 $L_\odot$ and a standard deviation of 0.05 $L_\odot$. The scatter increases as temperature increases. Dividing the sample into stars hotter and cooler than 4000 K, the luminosity differences for cooler sample have a median value of 0.005 $L_\odot$ and a standard deviation of 0.03 $L_\odot$ while the hotter sample has a median value of 0.034 $L_\odot$ and a standard deviation of 0.07 $L_\odot$. In the left panel of Figure 11, we display the adopted luminosities as a function of effective temperature.

Table 7
Equivalent Widths and Metallicities for Cool Dwarfs

		EW of Mg Features (A)						EW of Al Features (A)				Metallicity[a]			
		(1.50 μm)		(1.57 μm)		(1.71 μm)		a (1.67 μm)		b (1.67 μm)		[Fe/H]		[M/H]	
EPIC	Date	Val	Err	Val	Err	Val	Err	Val	Err	Val	Err	Val	Err	Val	Err
201205469	2015 Jun 13	5.84	0.37	3.82	0.30	3.59	0.33	2.43	0.21	3.01	0.23	0.433	0.166	0.307	0.146
201208431	2015 May 05	7.76	0.33	2.87	0.59	3.52	0.32	1.43	0.27	2.74	0.35	0.066	0.191	−0.024	0.170
201345483	2015 May 05	8.23	0.41	6.14	0.51	3.79	0.39	1.94	0.23	2.36	0.31	0.316	0.202	0.130	0.164
201549860	2015 Nov 26	8.13	0.10	5.08	0.10	3.86	0.09	1.72	0.07	2.15	0.09	…	…	…	…
201617985	2015 Apr 16	5.26	0.26	3.35	0.22	4.29	0.20	1.56	0.15	2.60	0.20	−0.010	0.143	−0.022	0.116
201635569	2015 May 05	7.44	0.39	5.13	0.30	5.02	0.36	2.08	0.20	2.92	0.25	0.196	0.180	0.138	0.147
201637175	2015 May 05	7.00	0.21	4.53	0.22	4.32	0.18	2.14	0.13	3.03	0.19	0.032	0.125	0.007	0.108
201717274	2015 May 05	2.28	0.32	1.06	0.32	1.42	0.32	1.52	0.23	2.10	0.26	−0.257	0.154	−0.188	0.132
201855371	2015 Apr 16	8.15	0.25	5.33	0.26	4.00	0.21	1.42	0.15	2.41	0.19	…	…	…	…
205924614	2015 Sep 24	8.30	0.22	5.81	0.20	4.17	0.17	1.39	0.13	2.17	0.16	0.246	0.125	0.170	0.108
205924614	2015 Nov 26	7.94	0.12	5.50	0.12	3.80	0.10	1.36	0.08	2.21	0.11	0.376	0.095	0.168	0.089
206011691	2015 Aug 07	8.13	0.08	5.60	0.08	4.42	0.07	1.66	0.06	2.33	0.09	−0.121	0.088	−0.122	0.085
206011691	2015 Sep 24	7.85	0.08	5.78	0.10	4.47	0.08	1.73	0.06	2.25	0.09	−0.034	0.090	−0.057	0.086
206119924	2015 Sep 24	8.34	0.07	5.68	0.08	3.88	0.06	1.52	0.06	2.25	0.08	0.337	0.086	0.204	0.084
206209135	2015 Sep 24	2.54	0.12	1.65	0.11	2.30	0.10	1.36	0.07	1.54	0.10	−0.271	0.093	−0.278	0.089
206312951	2015 Sep 24	4.95	0.11	3.28	0.11	3.10	0.09	1.64	0.07	2.39	0.08	0.097	0.092	0.066	0.087
206318379	2015 Sep 24	2.33	0.13	1.41	0.12	1.96	0.11	1.26	0.08	1.64	0.10	0.332	0.096	0.208	0.090
210448987	2015 Nov 27	7.41	0.10	4.88	0.10	3.14	0.09	1.39	0.07	1.59	0.10	…	…	…	…
210489231	2015 Sep 24	6.32	0.12	3.63	0.12	3.16	0.11	1.24	0.09	1.99	0.13	0.524	0.098	0.349	0.091
210508766	2015 Sep 24	5.82	0.08	4.28	0.09	3.95	0.08	1.72	0.07	2.21	0.09	−0.107	0.089	−0.060	0.085
210558622	2015 Oct 14	8.16	0.10	5.45	0.12	3.81	0.10	1.42	0.09	2.37	0.11	0.025	0.096	0.012	0.089
210558622	2015 Nov 26	8.21	0.11	5.58	0.11	3.76	0.10	1.22	0.08	2.14	0.11	0.094	0.094	0.050	0.090
210564155	2015 Nov 27	2.00	0.11	1.39	0.11	1.53	0.10	1.20	0.08	1.44	0.10	−0.149	0.092	−0.124	0.088
210707130	2015 Sep 24	8.48	0.07	5.71	0.07	3.84	0.06	1.57	0.06	2.22	0.09	…	…	…	…
210750726	2015 Sep 24	3.67	0.08	2.87	0.08	2.64	0.07	1.32	0.07	1.80	0.10	0.100	0.088	0.034	0.085
210838726	2015 Sep 24	5.28	0.06	3.55	0.08	3.51	0.07	1.63	0.05	2.21	0.07	0.180	0.085	0.111	0.083
210968143	2015 Sep 24	7.93	0.07	5.39	0.08	4.03	0.06	1.59	0.06	2.02	0.08	…	…	…	…
211077024	2015 Nov 26	2.96	0.08	1.73	0.08	1.79	0.08	1.22	0.05	1.62	0.07	0.170	0.087	0.062	0.085
211305568	2015 Nov 27	3.99	0.09	2.89	0.09	2.79	0.08	1.23	0.07	1.96	0.10	−0.175	0.090	−0.105	0.087
211331236	2015 Nov 26	4.68	0.10	2.97	0.10	3.05	0.09	1.59	0.07	2.02	0.10	0.037	0.091	0.083	0.088
211331236	2016 Apr 18	5.02	0.11	3.23	0.09	3.19	0.07	1.93	0.07	2.28	0.10	0.106	0.088	−0.001	0.085
211336288	2016 Mar 27	6.42	0.08	4.76	0.06	4.05	0.05	1.81	0.05	2.33	0.08	−0.075	0.084	−0.123	0.084
211357309	2015 Nov 27	4.49	0.10	3.23	0.10	2.88	0.09	1.65	0.08	2.03	0.11	−0.175	0.092	−0.085	0.088
211428897	2015 Nov 26	3.19	0.10	1.59	0.10	1.87	0.09	1.13	0.07	1.46	0.09	−0.131	0.087	−0.154	0.085
211509553	2016 Mar 27	5.77	0.17	3.64	0.11	4.03	0.09	2.17	0.07	2.83	0.11	0.044	0.096	−0.177	0.092
211680698	2016 Mar 28	7.44	0.14	4.87	0.09	2.77	0.07	1.15	0.07	1.56	0.09	…	…	…	…
211694226a	2016 Mar 8	4.13	0.18	2.98	0.17	2.83	0.17	1.67	0.12	2.74	0.13	0.043	0.108	0.053	0.101
211694226b	2016 Mar 8	3.54	0.24	2.75	0.22	2.39	0.24	1.71	0.15	2.42	0.16	0.261	0.131	0.117	0.110
211762841	2016 Mar 4	7.63	0.09	5.21	0.09	4.06	0.09	1.62	0.07	2.36	0.10	0.218	0.089	0.241	0.086
211770795	2016 Apr 18	7.38	0.17	5.35	0.12	3.27	0.09	1.33	0.07	1.54	0.10	…	…	…	…
211791178	2016 Mar 27	7.30	0.15	4.79	0.11	3.24	0.09	1.26	0.06	1.79	0.07	−0.399	0.096	−0.095	0.092
211799258	2016 Mar 8	3.58	0.39	2.18	0.32	1.15	0.35	0.73	0.23	1.07	0.25	0.120	0.167	0.181	0.145
211817229	2016 Mar 4	1.23	0.12	0.90	0.11	0.95	0.11	0.63	0.08	0.62	0.11	−0.401	0.090	−0.327	0.088
211818569	2016 Feb 19	7.66	0.10	5.30	0.08	3.22	0.06	1.12	0.06	1.73	0.09	…	…	…	…
211822797	2016 Mar 27	6.41	0.08	4.64	0.07	3.94	0.06	1.90	0.05	2.08	0.07	0.322	0.084	0.179	0.083
211826814	2016 Feb 19	2.60	0.35	0.97	0.27	1.33	0.21	0.63	0.15	1.06	0.19	−0.254	0.130	−0.317	0.123
211831378	2016 Apr 18	5.47	0.40	3.91	0.23	3.76	0.19	1.88	0.13	2.60	0.16	0.257	0.138	0.111	0.128
211839798	2016 Mar 4	1.69	0.12	1.18	0.12	1.48	0.12	0.92	0.08	0.98	0.11	−0.078	0.095	−0.010	0.089
211924657	2016 Mar 8	2.42	0.13	1.69	0.13	1.72	0.13	1.01	0.09	1.32	0.11	−0.004	0.096	−0.006	0.091
211965883	2016 Mar 27	7.40	0.08	5.10	0.07	4.16	0.05	1.86	0.04	2.33	0.06	−0.196	0.084	0.024	0.083
211969807	2016 Mar 8	3.87	0.25	3.47	0.21	3.26	0.23	1.73	0.15	2.67	0.18	0.179	0.125	0.200	0.116
211970234	2016 Apr 18	1.46	0.28	1.08	0.16	1.22	0.13	1.05	0.09	0.83	0.12	−0.177	0.109	−0.087	0.102
211988320	2016 Mar 27	7.20	0.08	5.13	0.06	4.20	0.04	1.50	0.04	1.97	0.06	−0.369	0.084	−0.157	0.083
212006344	2015 Nov 26	7.30	0.07	4.95	0.07	4.35	0.06	1.99	0.06	2.86	0.08	0.444	0.085	0.341	0.083
212006344	2016 Feb 19	7.25	0.10	5.38	0.09	4.12	0.06	2.37	0.06	3.15	0.08	0.521	0.086	0.309	0.085
212069861	2015 Nov 26	7.08	0.08	4.64	0.08	3.90	0.07	1.75	0.06	2.38	0.09	0.324	0.088	0.195	0.085
212154564	2016 Mar 27	3.35	0.11	2.00	0.10	2.63	0.07	1.14	0.05	1.64	0.07	−0.093	0.088	−0.238	0.086
212354731	2016 Mar 28	3.36	0.30	2.61	0.17	2.13	0.15	1.39	0.11	1.79	0.11	−0.009	0.124	0.018	0.107
212398486	2016 Mar 4	4.09	0.16	2.58	0.15	2.50	0.17	1.58	0.10	1.61	0.12	−0.278	0.103	−0.197	0.096
212443973	2016 Mar 27	2.31	0.08	1.99	0.06	2.44	0.05	1.12	0.05	1.32	0.08	0.201	0.084	−0.054	0.083
212460519	2016 Mar 8	7.57	0.11	4.77	0.12	3.68	0.11	1.42	0.10	1.71	0.13	−0.116	0.095	−0.140	0.091

Table 7
(Continued)

		EW of Mg Features (A)						EW of Al Features (A)				Metallicity[a]			
		(1.50 μm)		(1.57 μm)		(1.71 μm)		a (1.67 μm)		b (1.67 μm)		[Fe/H]		[M/H]	
EPIC	Date	Val	Err	Val	Err	Val	Err	Val	Err	Val	Err	Val	Err	Val	Err
212554013	2016 Apr 18	6.85	0.22	4.79	0.15	2.86	0.12	1.36	0.09	1.84	0.11	…	…	…	…
212565386	2016 Mar 10	6.09	0.14	4.23	0.14	2.97	0.14	1.30	0.10	1.88	0.13	0.020	0.103	−0.002	0.095
212572452	2016 Mar 10	8.64	0.18	6.09	0.17	4.44	0.16	1.55	0.13	2.37	0.18	0.206	0.112	0.184	0.102
212572452	2016 Mar 27	8.77	0.31	5.78	0.38	4.16	0.22	1.52	0.19	1.77	0.24	0.249	0.131	0.222	0.124
212628098	2016 Apr 18	6.89	0.15	4.63	0.12	3.13	0.08	1.83	0.07	2.75	0.10	−0.008	0.093	0.015	0.088
212634172	2016 Mar 4	2.47	0.13	1.79	0.13	1.67	0.12	1.07	0.09	1.24	0.11	0.405	0.096	0.299	0.092
212679181	2016 Mar 4	3.72	0.11	2.89	0.12	2.70	0.10	1.29	0.08	1.70	0.11	0.084	0.092	0.027	0.089
212679798	2016 Apr 18	6.08	0.22	4.44	0.16	3.08	0.12	1.82	0.10	2.77	0.15	0.402	0.104	0.296	0.097
212686205	2016 Mar 8	7.51	0.10	4.97	0.11	3.22	0.10	0.95	0.10	1.54	0.15	…	…	…	…
212690867	2016 Mar 8	3.56	0.18	2.62	0.18	3.07	0.18	1.59	0.15	2.11	0.20	−0.188	0.114	−0.187	0.104
212773272	2016 Apr 18	2.79	0.18	2.32	0.12	2.08	0.11	1.68	0.07	2.36	0.10	0.329	0.098	0.250	0.092
212773309	2016 Mar 28	6.87	0.09	4.72	0.08	3.28	0.05	1.53	0.05	2.10	0.08	0.288	0.085	0.123	0.084
212773309B	2016 Mar 28	3.37	0.33	2.07	0.20	2.62	0.17	1.61	0.11	2.20	0.14	0.595	0.144	0.251	0.115
213951550	2016 May 6	4.84	0.17	3.23	0.15	3.15	0.15	1.58	0.11	2.66	0.13	0.153	0.110	0.099	0.097
214254518	2016 May 5	7.57	0.08	5.09	0.09	3.75	0.08	1.38	0.07	1.95	0.09	−0.074	0.090	−0.055	0.086
214254518	2016 Oct 26	8.00	0.08	5.53	0.09	3.73	0.07	1.30	0.07	1.73	0.10	−0.130	0.089	−0.058	0.086
214522613	2016 May 5	4.35	0.21	2.90	0.20	2.93	0.19	1.73	0.13	2.45	0.17	0.407	0.118	0.125	0.106
214787262	2016 May 5	2.70	0.09	1.96	0.09	1.89	0.08	0.99	0.06	1.32	0.08	0.006	0.089	0.023	0.086
216892056	2016 May 5	2.94	0.10	2.31	0.11	2.50	0.10	1.52	0.08	1.85	0.11	−0.111	0.093	−0.116	0.089
217941732	2016 May 5	7.26	0.24	5.05	0.22	3.86	0.23	1.08	0.17	1.69	0.20	…	…	…	…
217941732	2016 Oct 26	7.03	0.23	5.08	0.23	4.21	0.21	1.37	0.16	1.95	0.20	…	…	…	…

Note.
[a] Estimated by taking the average of the *H*-band and *K*-band estimates determined using the spectral indices introduced by Mann et al. (2013a). We do not report [Fe/H] and [M/H] for K3–K5 dwarfs because the Mann et al. (2013a) relations are not valid for those stars.

4.2.5. Stellar Masses

The Newton et al. (2015) relations do not include masses, so we computed the masses for all stars using the stellar effective temperature–mass relation from Mann et al. (2013b). The right panel of Figure 11 displays the resulting mass estimates as a function of stellar radius.

4.3. Adopted Properties

After checking that the results from both classification schemes are generally consistent, we adopted parameters based on the Newton et al. (2015) relations when possible because the calibrations are valid for hotter stars (3100–4800 K versus 2700–4100 K), and because EWs are less susceptible to telluric contamination than the indices used by Mann et al. (2013b). Furthermore, the Mann et al. (2013b) temperature calibrations have inflection points while the Newton et al. (2015) relations do not.

Specifically, we report temperatures, radii, and luminosities estimated using the Newton et al. (2015) relations, metallicities based on the Mann et al. (2013a) relations, masses generated by running the Newton temperatures through the temperature–mass relation from Mann et al. (2013b), and surface gravities computed from the radii and masses. (The exceptions are EPIC 211817229, EPIC 211799258, and EPIC 211826814, for which we adopt the Mann parameters, as explained in Section 4.2.3.) The Newton et al. (2015) relations are not valid for early K dwarfs, so we rejected all of the stars with assigned temperatures hotter than 4800 K or radii larger than 0.8 $R_\odot$.

As shown in the left panel of Figure 12, our cool dwarf sample has a median radius of 0.56 $R_\odot$. The temperature distribution in the right panel is bimodal, featuring a peak near 3500 K from the mid-M dwarfs in the sample and a second peak near 4350 K from late K dwarfs. The median value of the distribution is 3884 K.

Our final cool dwarf sample consists of 74 stars in 72 systems; EPIC 211694226 and EPIC 212773309 are visual binaries. We obtained spectra of both components and consider all four stars as possible planetary host stars. As of 2016 August 24, there were no AO images of either system posted on the ExoFOP-K2 follow-up website. Using our data, we measured separations of roughly 1.″7 and 11.″3, respectively. The companion star to EPIC 212773309 is likely 2MASS J13493168–0619267, which is listed on the ExoFOP-K2 website[14] at a separation of 11.″4. 2MASS J13493168–0619267 is 2.6 *Kp* magnitudes fainter than EPIC 212773309 and far enough away to lie outside of the K2 target aperture. In contrast, both stars in the EPIC 211694226 system could fall within a single 3.″98 K2 pixel.

The adopted parameters for the EPIC 211694226 and EPIC 212773309 visual binaries and all of the other stars in our cool dwarf sample are reported in Table 6. For reference, we also provide the intermediate measurements in Table 7 along with our metallicity estimates.

As shown in Figure 13, three of the stars in our cool dwarf sample were initially classified as giants in the EPIC. Considering only the stars originally classified as dwarfs, the median changes between our revised estimates and the EPIC values are +0.13 $M_\odot$ (+26%), +0.13 $R_\odot$ (+39%), and −4 K

[14] https://exofop.ipac.caltech.edu/k2/edit_target.php?id=212773309

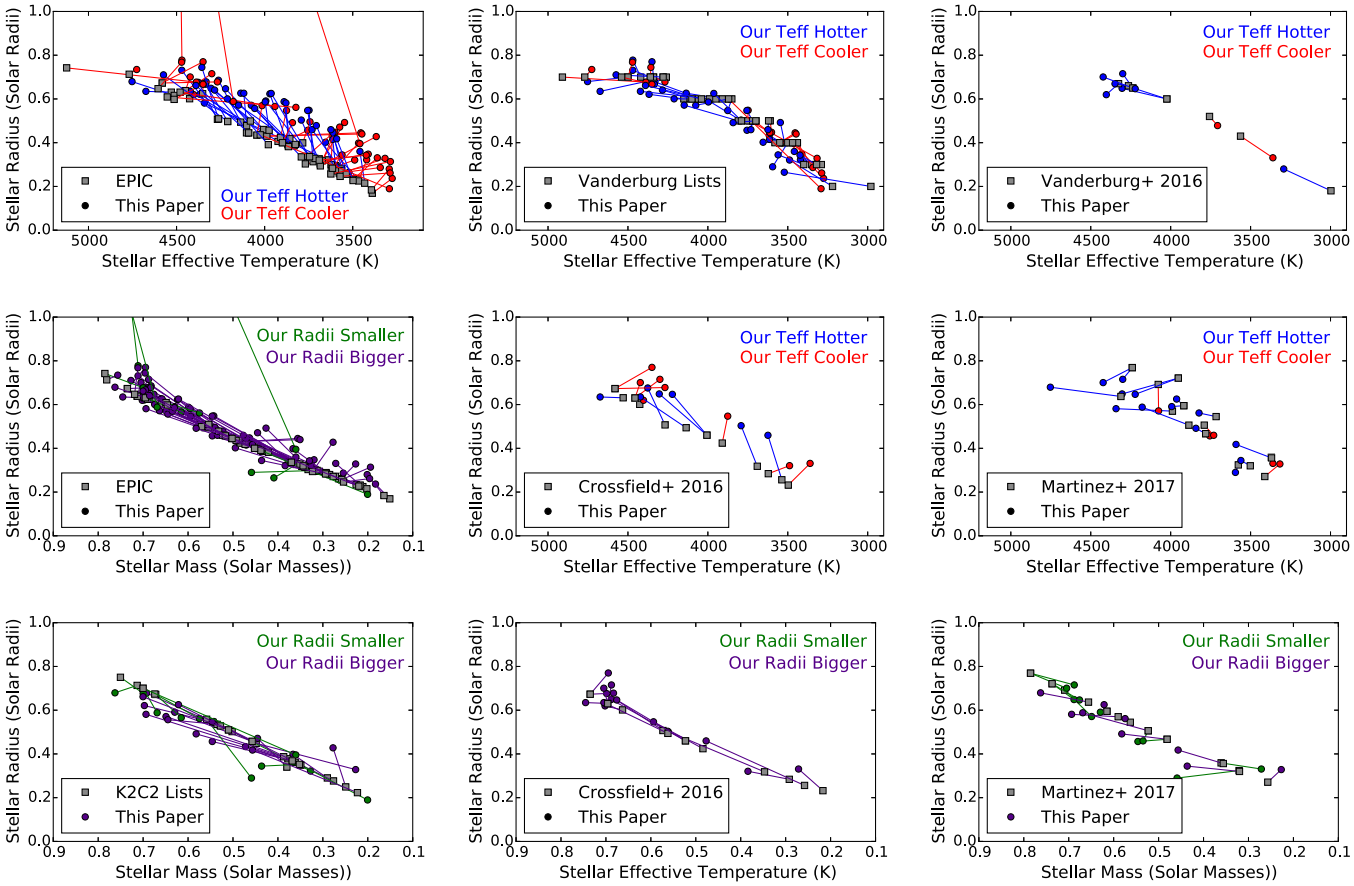

Figure 13. Comparison of our revised stellar parameters (circles) to the earlier estimates from other studies (gray squares). Solid lines connect the before and after values for each star. Top left: stellar radius vs. effective temperature comparing values in the EPIC to our updated values. In this panel and in all other radius vs. temperature panels, blue (red) lines connect the initial and revised values for stars for which our new effective temperature estimates are hotter (cooler). Top center: stellar radius vs. stellar effective temperature comparing values in the unpublished planet candidate lists provided by A. Vanderburg to our updated values. Top right: stellar radius vs. stellar effective temperature comparing values in Vanderburg et al. (2016) to our updated values. Middle center: stellar radius vs. stellar effective temperature comparing values in Crossfield et al. (2016) to our updated values. Middle right: stellar radius vs. stellar effective temperature comparing values in Martinez et al. (2017) to our updated values. Bottom left: stellar radius vs. stellar mass comparing values in unpublished K2C2 planet candidate lists to our updated values. Bottom center: stellar radius vs. stellar mass comparing values in Crossfield et al. (2016) to our updated values. Bottom right: stellar radius vs. stellar mass comparing values in Martinez et al. (2017) to our updated values.

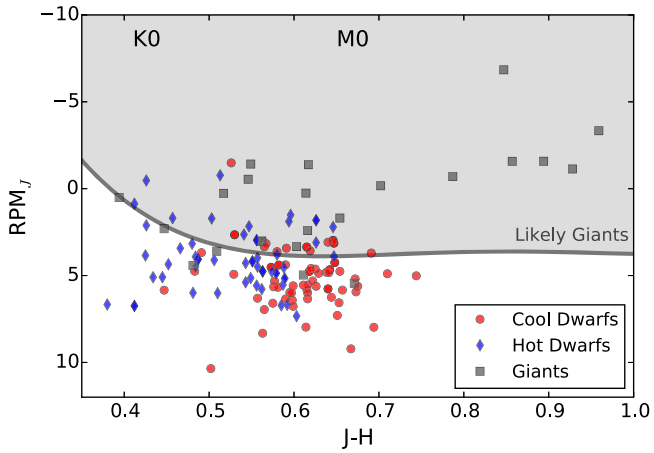

Figure 14. Reduced proper motion in J band vs. $J - H$ for all of the stars we observed and later classified as giants (gray squares), hotter dwarfs (blue diamonds), or cool dwarfs (red circles). The gray line marks the dwarf/giant cut suggested by Collier Cameron et al. (2007); stars lying above this line (in the gray shaded region) are more likely to be giants while targets below the line are more likely to be dwarfs. For reference, we note the approximate $J - H$ colors of K0 and M0 stars.

(−0.1%). For the 15 cool dwarfs with previous published estimates in Crossfield et al. (2016), we find median changes of +0.09 $M_\odot$ (+23%), +0.10 $R_\odot$ (+28%), and −23 K (−0.5%). We find smaller radius changes (+0.05 $R_\odot$, +8%) but larger temperature changes (+84 K, +2%) for the nine cool dwarfs with earlier estimates from Vanderburg et al. (2016). Consulting the unpublished planet candidate lists in which the stellar parameters are only coarsely estimated, we find median changes of +0.02 $R_\odot$ (+4%) and +65 K (+2%) for the 56 cool dwarfs in lists provided by A. Vanderburg and +0.08 $M_\odot$ (+22%) and +0.07 $R_\odot$ (+17%) for the 28 cool dwarfs in lists from the K2C2 Consortium.

Martinez et al. (2017) recently completed a parallel study in which they estimated the properties of low-mass K2 planet host stars using NTT/SOFI spectra covering the 0.95–2.52 μm wavelength range. Although their spectra are lower resolution than our data ($R \sim 1000$ rather than $R \sim 2000$–2700, they report consistent parameters for most of the 15 stars observed by both studies. Specifically, the median differences between our estimates (Dressing–Martinez) are 61 K, 0.01 $M_\odot$, and −0.004 $R_\odot$.

5. Discussion and Conclusions

In this paper, we presented revised system parameters for 144 targets observed by the NASA K2 mission. All of those stars were initially suspected to be cool dwarfs harboring transiting planets, but some of these systems have since been revealed to be false positives. Comparing our IRTF/SpeX and Palomar/TripleSpec spectra to standard spectra from the IRTF Spectral Library (Rayner et al. 2009), we found that 49% of our targets were contaminating giants or hotter dwarfs.

Intriguingly, one star (EPIC 211817229) has large proper motion (380 mas yr^{-1} Roeser et al. 2010) and moderate radial velocity (28 Km s^{-1}), indicating that the star likely does not belong to the thin disk population. Accordingly, we used the measured position, proper motion, and radial velocity of EPIC 211817229 along with an estimated photometric distance of 55 ± 10 pc (Pecaut & Mamajek 2013), to calculate the star's *UVW* Galactic velocities corrected for the Sun's velocity (Coşkunoğlu et al. 2011). We estimated $(UVW)_{\rm LSR} = (-11 \pm 9, -88 \pm 17, -15 \pm 8)$ km s^{-1}.

We then compared the Galactic velocities of EPIC 211817229 to distributions proposed in Bensby et al. (2014) that approximately define the thin disk, thick disk, and halo populations. The total Galactic velocity of EPIC 211817229, $V_{\rm tot} = 90 \pm 21$ km s^{-1}, is consistent with the thick disk population ($V_{\rm tot}$ 70–180 km s^{-1}). The placement of the star in a Toomre diagram and the estimated probability of membership in the three populations (Bensby et al. 2014, Appendix A) also point to a star in the thick disk. This kinematic classification is consistent with EPIC 211817229 being metal-poor and suggests an old age.

After classifying all of our targets, we revisited the initial selection of our sample to ask whether we could better identify low-mass stars in the future. As shown in the *J*-band reduced proper motion (RPM_J) versus $J - H$ color plot in Figure 14, one possible avenue for improvement is to impose stricter cuts on the $J - H$ color and reduced proper motions of the target stars. For instance, confining our follow-up sample to stars with $0.45 < J - H < 0.8$ would have decreased the giant contamination by 30% and hot dwarf contamination by 18% while excluding only one cool dwarf from our sample. Imposing a further cut of $RPM_J > 1$ would decrease giant contamination by an additional 35% and hot dwarf contamination by an additional 2% at the cost of excluding two more cool dwarfs. Employing the more complicated polynomial cut suggested by Collier Cameron et al. (2007) would remove 74% of the giants and 29% of the hot dwarfs along with 31% of the cool dwarfs.

The main focus of this work was the sample of 74 cool dwarfs with spectral types between K3 and M4. For those stars, we estimated temperatures, radii, masses, luminosities, and metallicities using empirical relations (Mann et al. 2013a, 2013b, 2015; Newton et al. 2015). In most cases, we found that the original radius estimates were smaller than the actual radii of the stars: our revised estimates are typically 0.13 $R_\odot$ (39%) larger than the values reported in the EPIC (Huber et al. 2016), 0.10 $R_\odot$ (28%) larger than the values in Crossfield et al. (2016), and 0.05 $R_\odot$ (8%) larger than those in Vanderburg et al. (2016).

We defer a detailed discussion of the planetary implications of our revisions to the stellar parameters to the next paper in this series (C. D. Dressing et al. 2017, in preparation), but assuming that the initial planet/star radius ratios are correct, we predict that the associated planet candidates are also 10%–30% larger than initially estimated. Accordingly, potentially habitable Earth-sized planets orbiting stars originally believed to be small, cool M dwarfs may be larger and significantly less habitable than previously inferred. This result underscores the importance of characterizing TESS planet host stars before acquiring detailed atmospheric observations with *JWST* and the next-generation of extremely large ground-based telescopes.

Many of our targets were provided by the K2 California Consortium (K2C2). We thank K2C2 for sharing their candidate lists and vetting products. In particular, we thank K2C2 members Ian Crossfield and Arturo Martinez for their willingness to coordinate follow-up observations of low-mass stars. We are grateful to Michael Cushing for sharing a beta version of the Spextool pipeline designed for TripleSpec data. We thank Philip Muirhead and Juliette Becker for providing advice regarding TripleSpec data acquisition and reduction. We also acknowledge helpful conversations with Chas Beichman and Eric Gaidos. We thank Andrew Howard for donating SpeX time and Kimberly Aller, Will Best, and Michael Liu for obtaining some of the SpeX observations described in this paper. Finally, we thank the anonymous referee for providing feedback that improved the quality of this paper.

This work was performed under contract with the Jet Propulsion Laboratory (JPL) funded by NASA through the Sagan Fellowship Program executed by the NASA Exoplanet Science Institute. This publication was made possible through the support of a grant from the John Templeton Foundation. The opinions expressed here are those of the authors and do not necessarily reflect the views of the John Templeton Foundation. This paper includes data collected by the K2 mission, which is funded by the NASA Science Mission directorate. Our follow-up observations were obtained at the IRTF, which is operated by the University of Hawaii under contract NNH14CK55B with the National Aeronautics and Space Administration and at Palomar Observatory. We thank the staff at both observatories and the Caltech Remote Observing Facilities staff for supporting us during our many observing runs. We are grateful to the IRTF and Caltech TACs for awarding us telescope time. This research has made use of the NASA Exoplanet Archive, which is operated by the California Institute of Technology, under contract with the National Aeronautics and Space Administration under the Exoplanet Exploration Program.

The authors wish to recognize and acknowledge the very significant cultural role and reverence that the summit of Mauna Kea has always had within the indigenous Hawaiian community. We are most fortunate to have the opportunity to conduct observations from this mountain.

Facilities: IRTF (SpeX), Palomar (TripleSpec).

Appendix
Reduced Stellar Spectra

As mentioned in Section 4.1, all of our reduced spectra have been posted on the ExoFOP website. We also display the spectra in Figures 15–20 for cool dwarfs, Figures 21–23 for hotter dwarfs, and Figures 24–25 for giants.

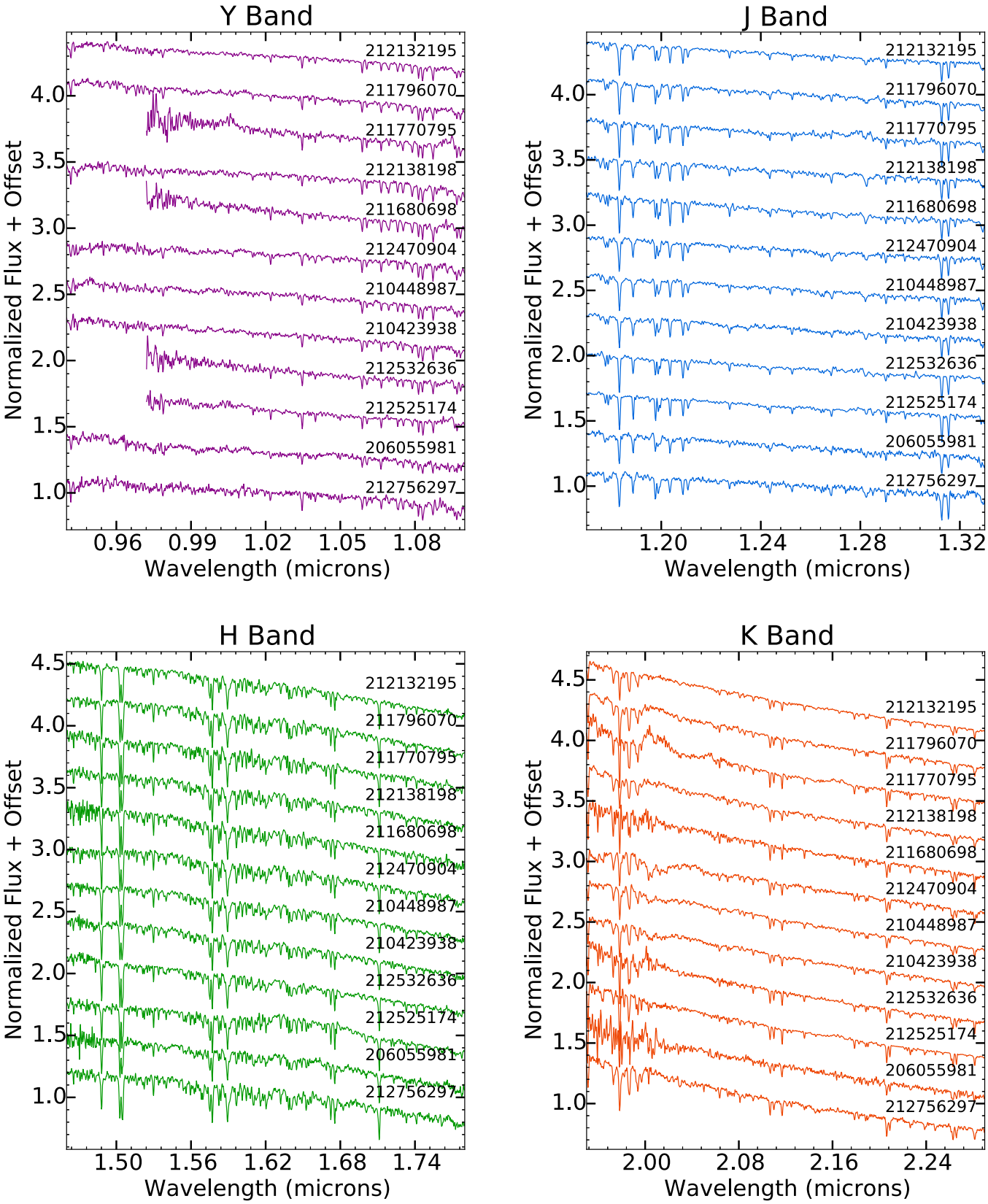

Figure 15. *Y*-band (top left), *J*-band (top right), *H*-band (bottom left), and *K*-band (bottom right) spectra of cool dwarfs with effective temperatures between 4800 and 4480 K. The hottest stars are shown at the top of the plots. Stars with truncated *Y*-band coverage were observed at the Palomar 200″ Hale Telescope using TripleSpec; the other stars were observed at the IRTF using SpeX.

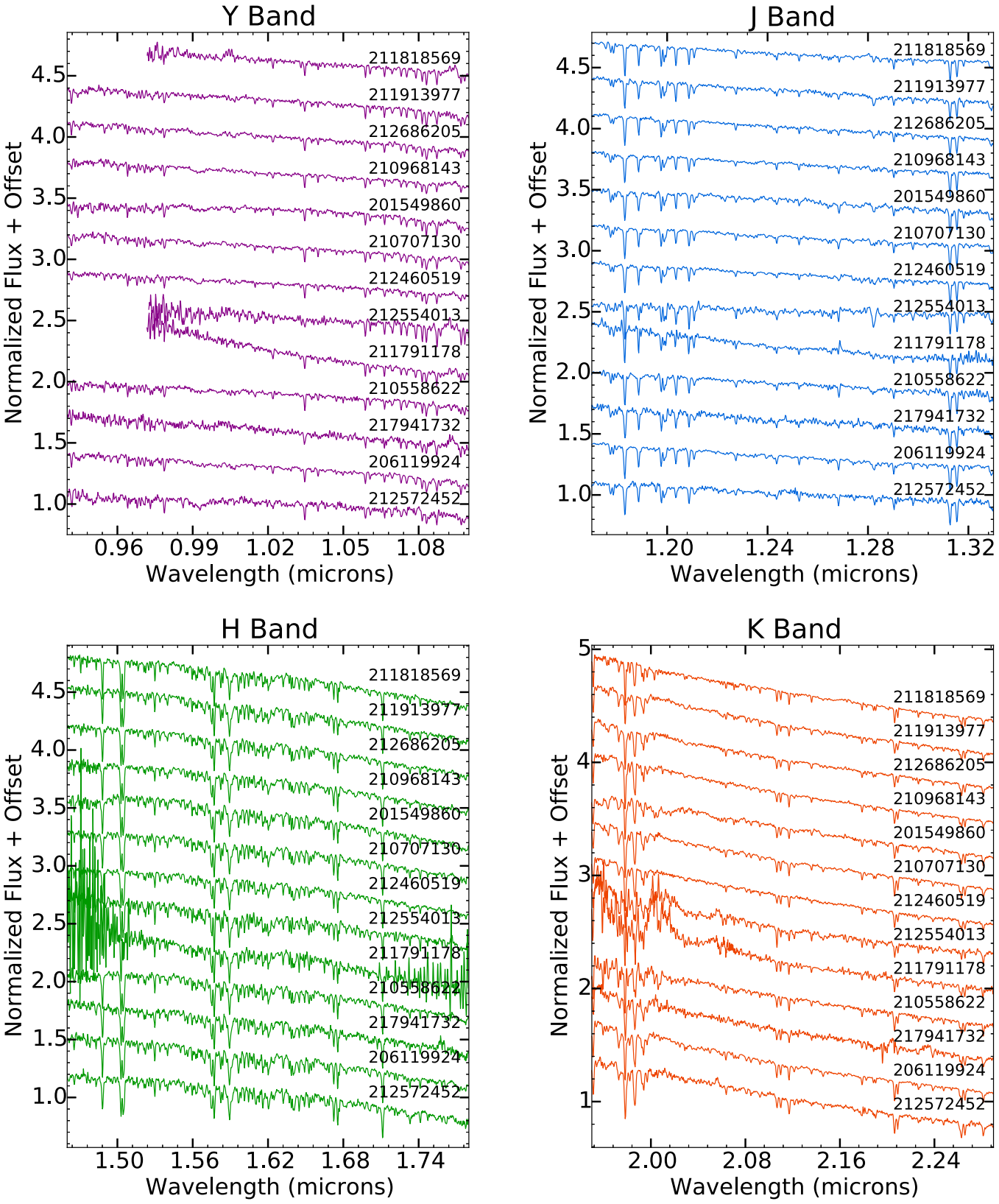

Figure 16. Same as Figure 15 for cool dwarfs with effective temperatures between 4480 and 4333 K.

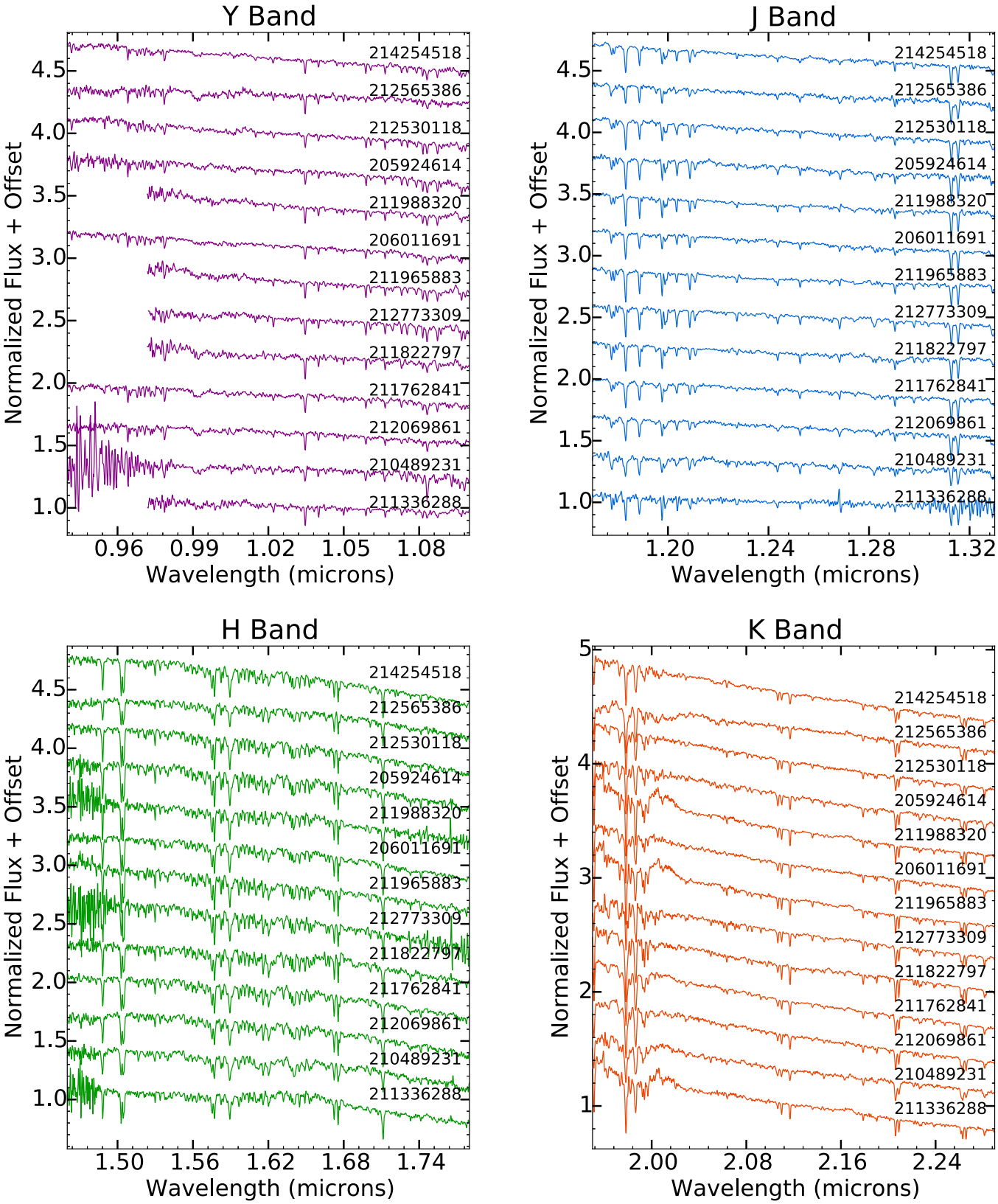

Figure 17. Same as Figure 15 for cool dwarfs with effective temperatures between 4333 and 3995 K.

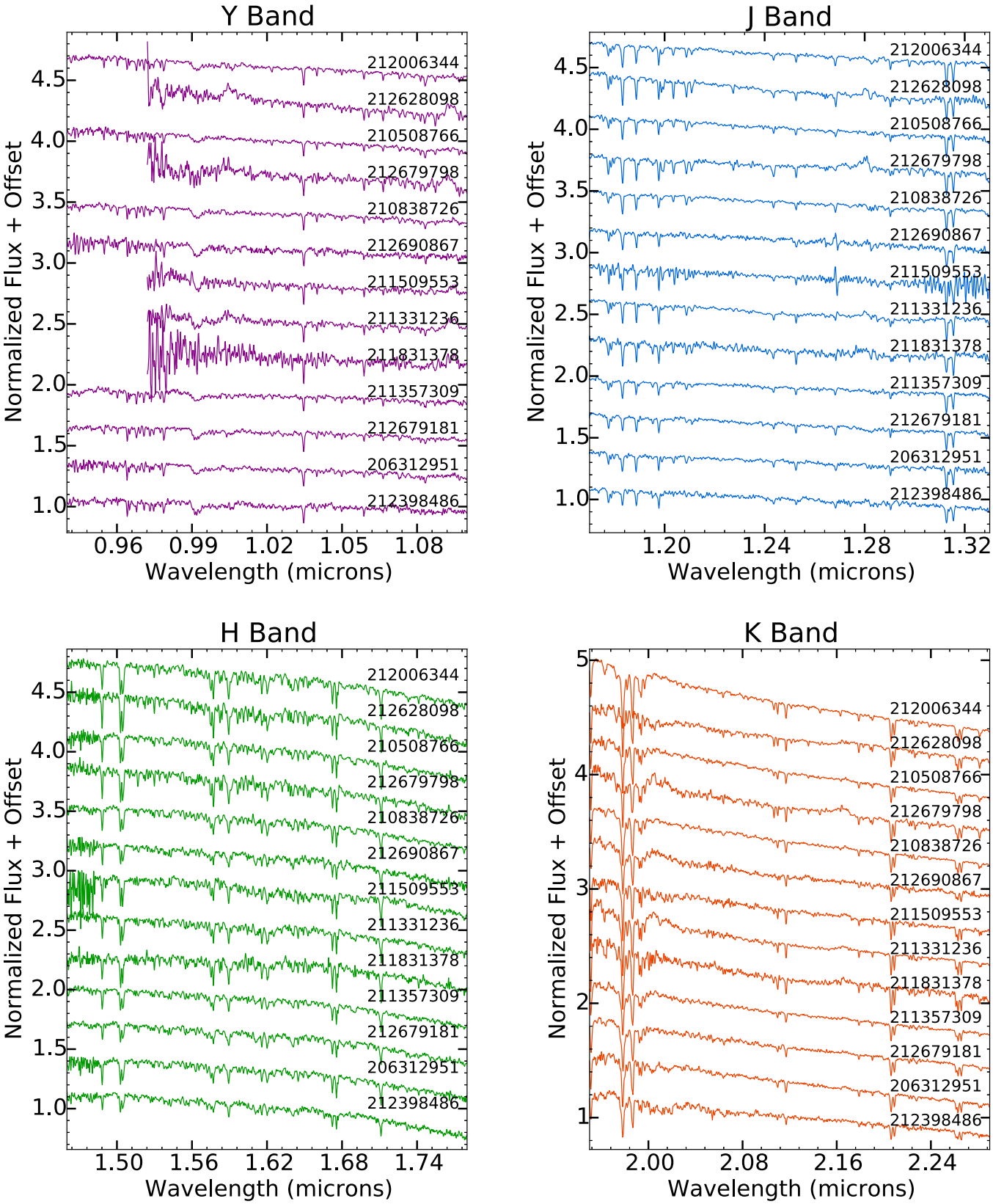

Figure 18. Same as Figure 15 for cool dwarfs with effective temperatures between 3995 and 3650 K.

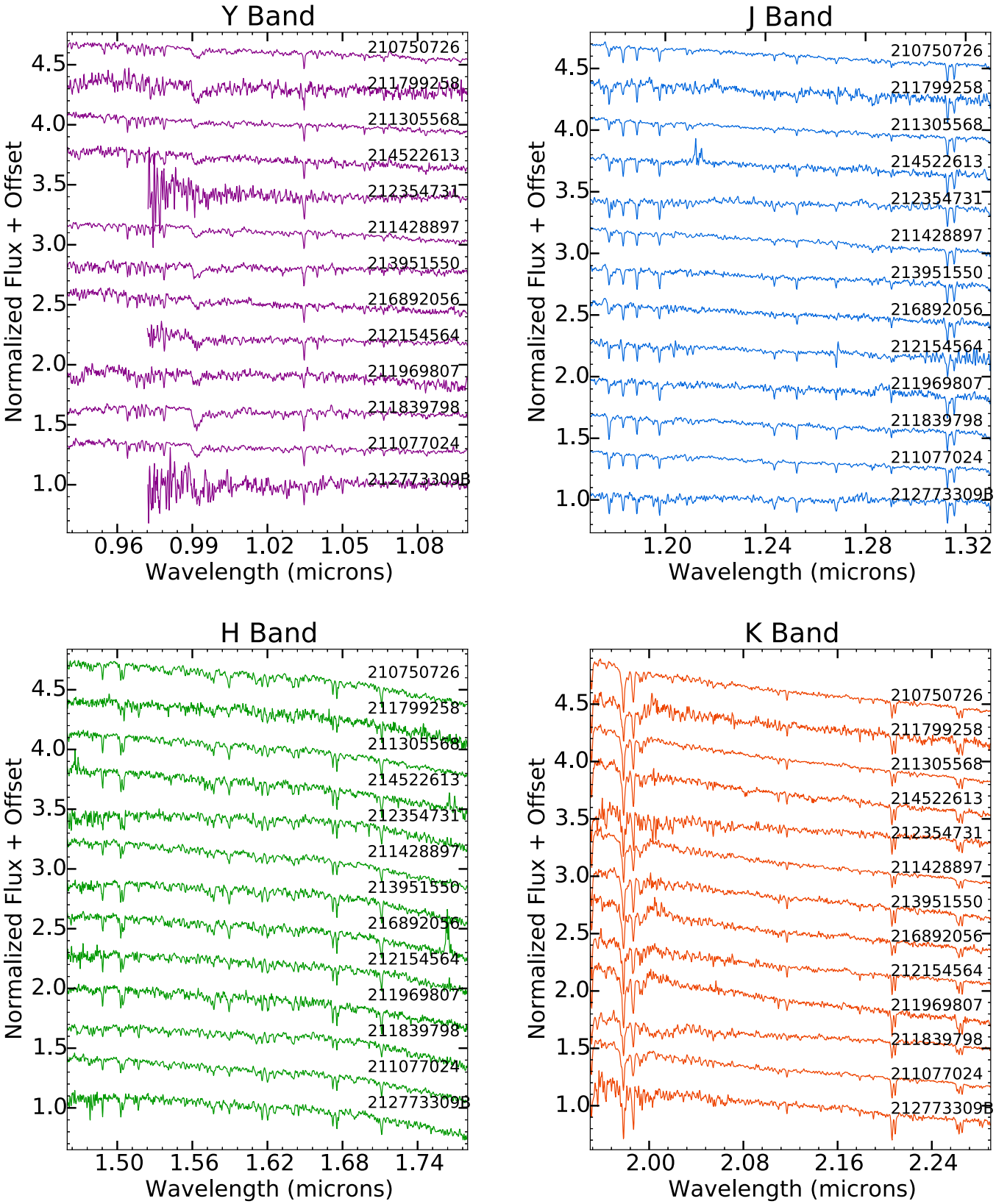

Figure 19. Same as Figure 15 for cool dwarfs with effective temperatures between 3650 and 3465 K.

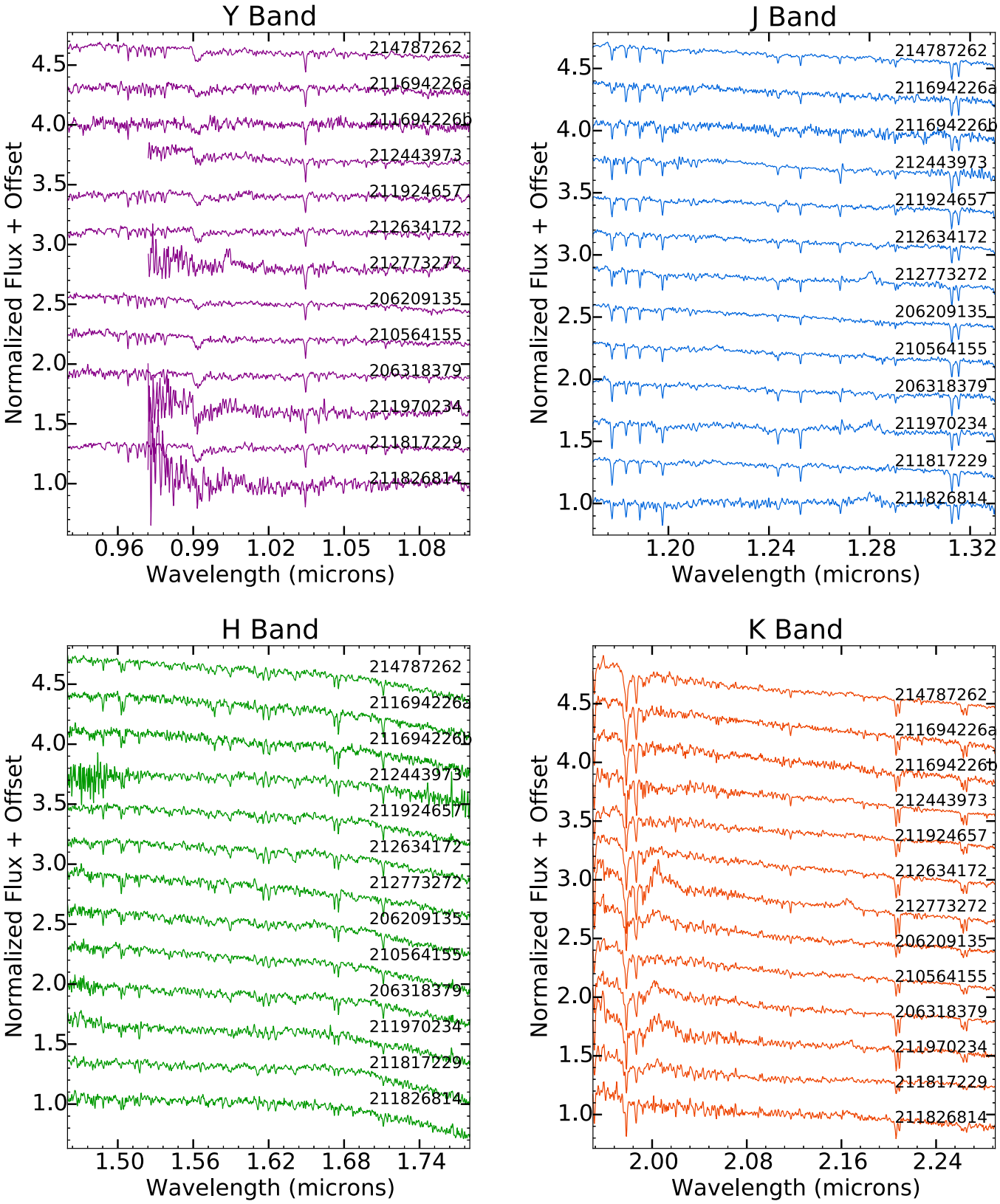

Figure 20. Same as Figure 15 for cool dwarfs with effective temperatures between 3465 and 3220 K.

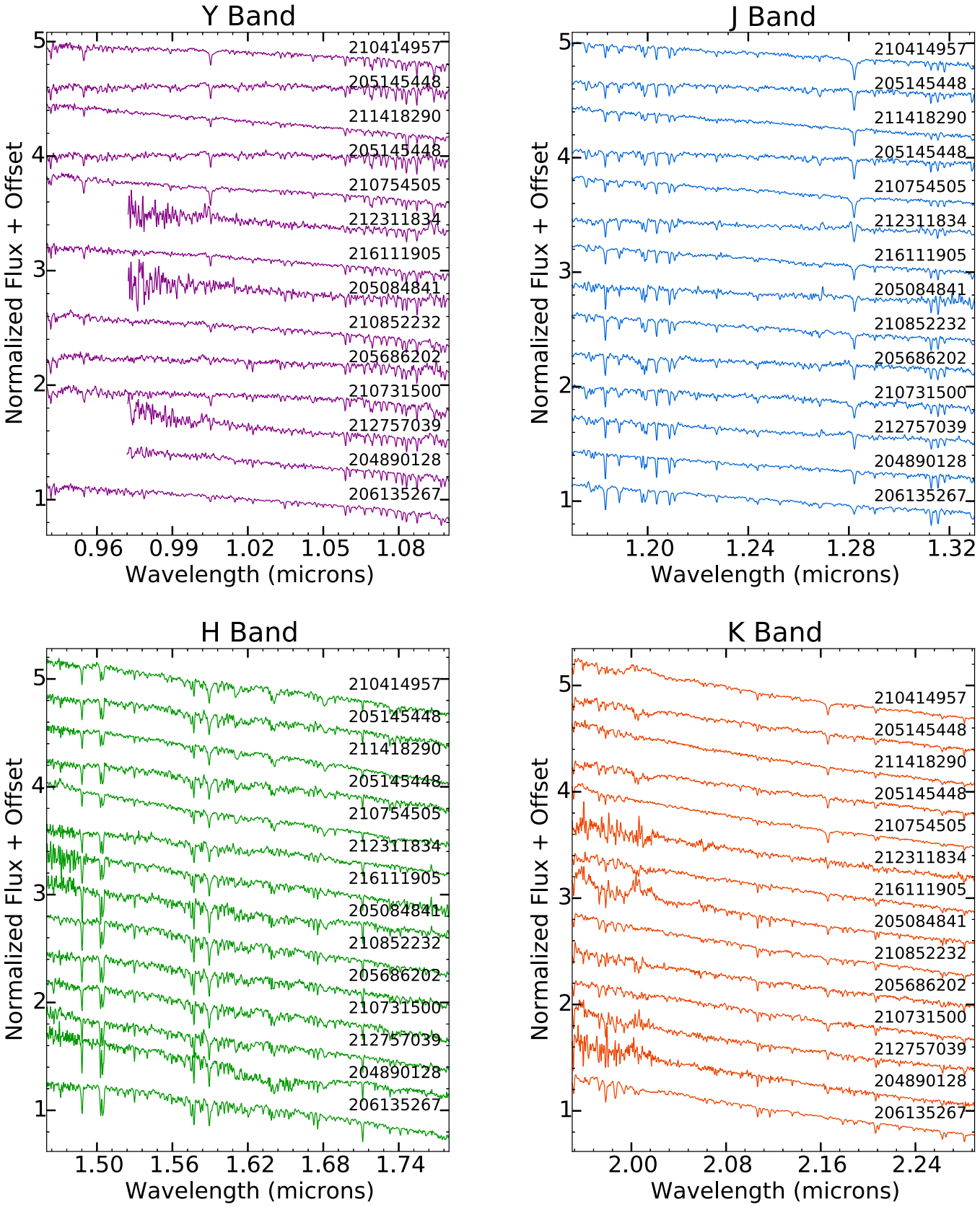

Figure 21. *Y*-band (top left), *J*-band (top right), *H*-band (bottom left), and *K*-band (bottom right) spectra of hotter dwarfs with spectral types between K2 and G2. The hottest stars are shown at the top of the plots. Stars with truncated *Y*-band coverage were observed at the Palomar 200″ Hale Telescope using TripleSpec; the other stars were observed at the IRTF using SpeX.

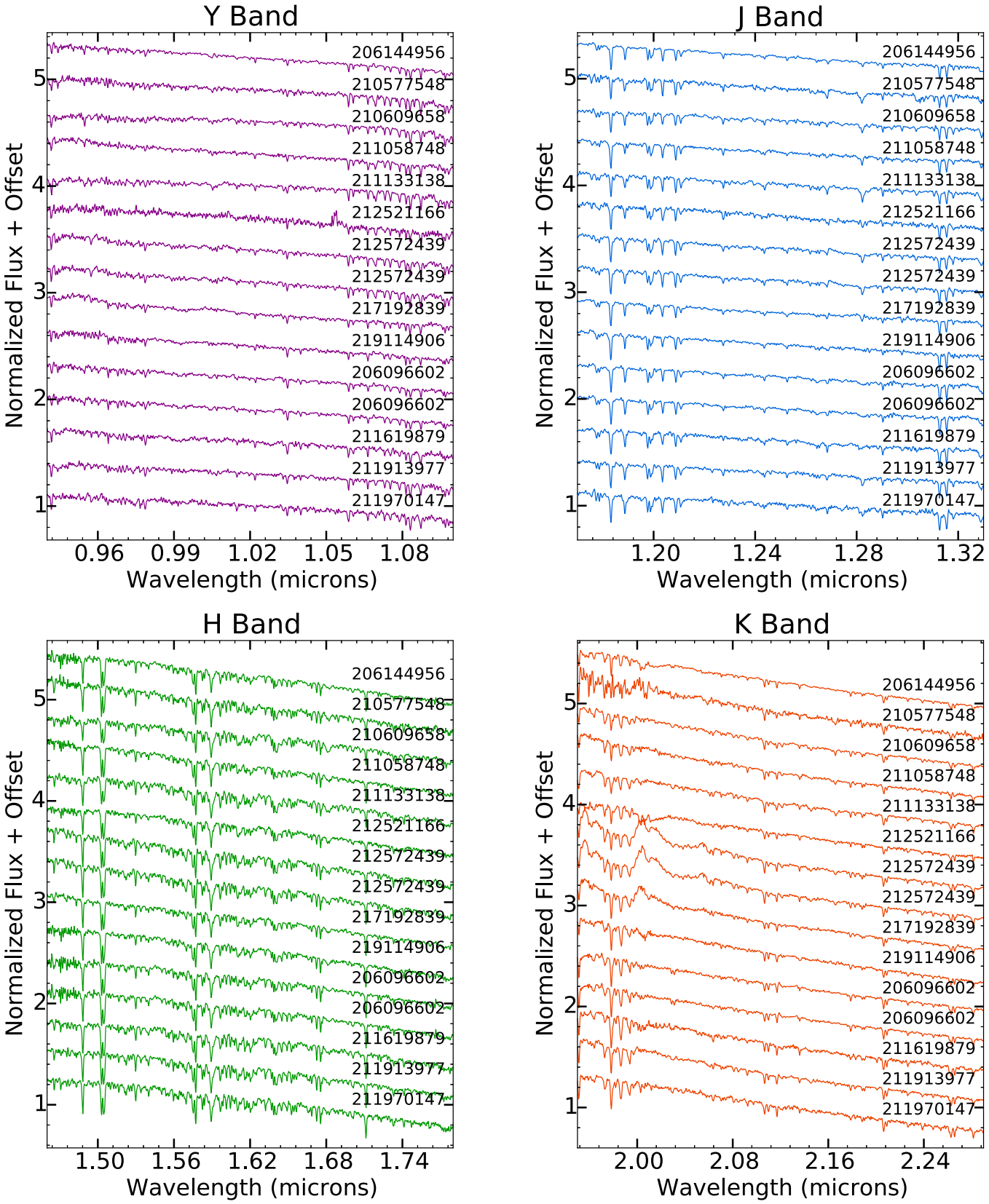

Figure 22. Same as Figure 21 for hotter dwarfs with spectral types between K3 and K2.

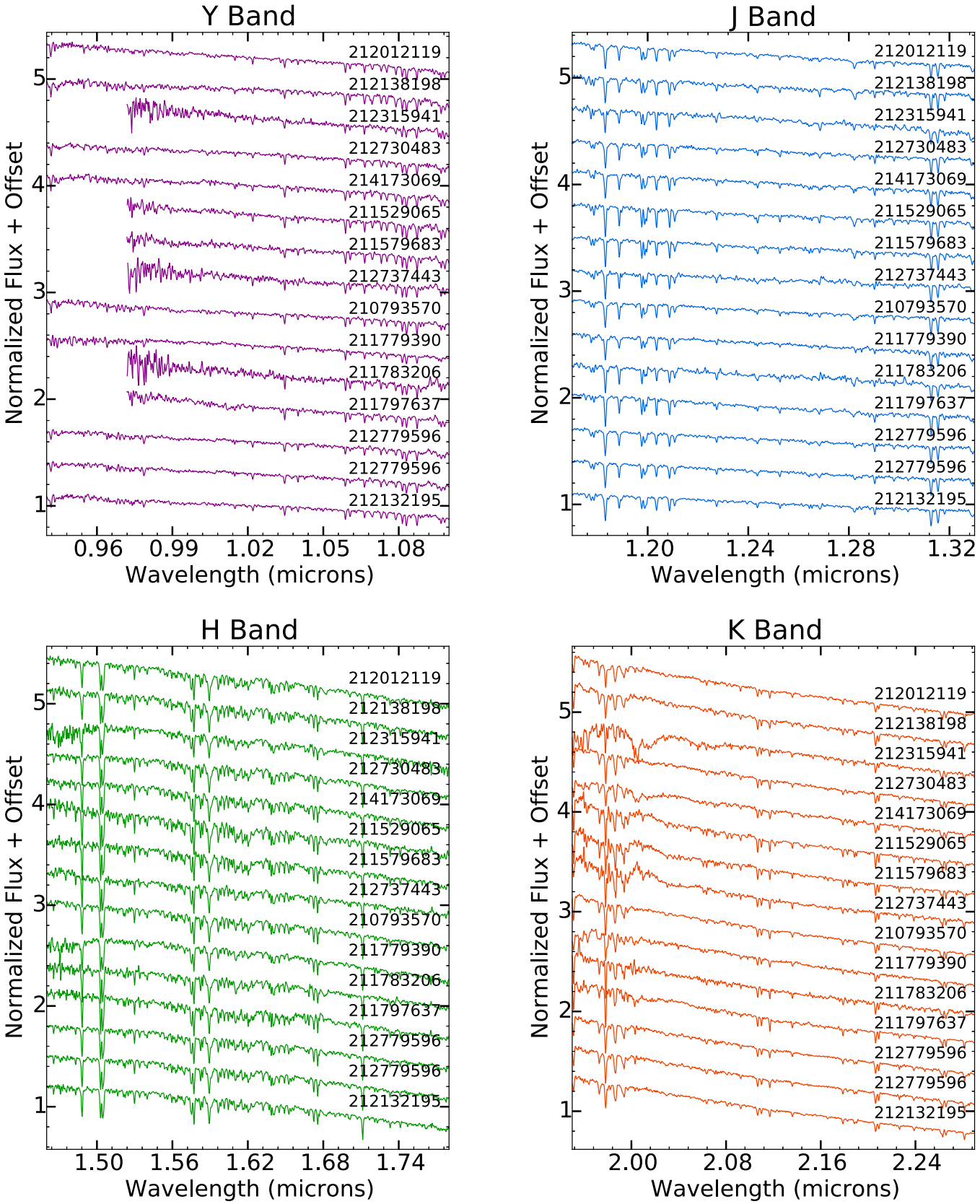

Figure 23. Same as Figure 21 for hotter dwarfs with spectral types between K5 and K3. Although some of these stars were expected to be cool enough for the Newton et al. (2015) relations, they were assigned temperatures hotter than 4800 K and were therefore excluded from the cool dwarf analysis.

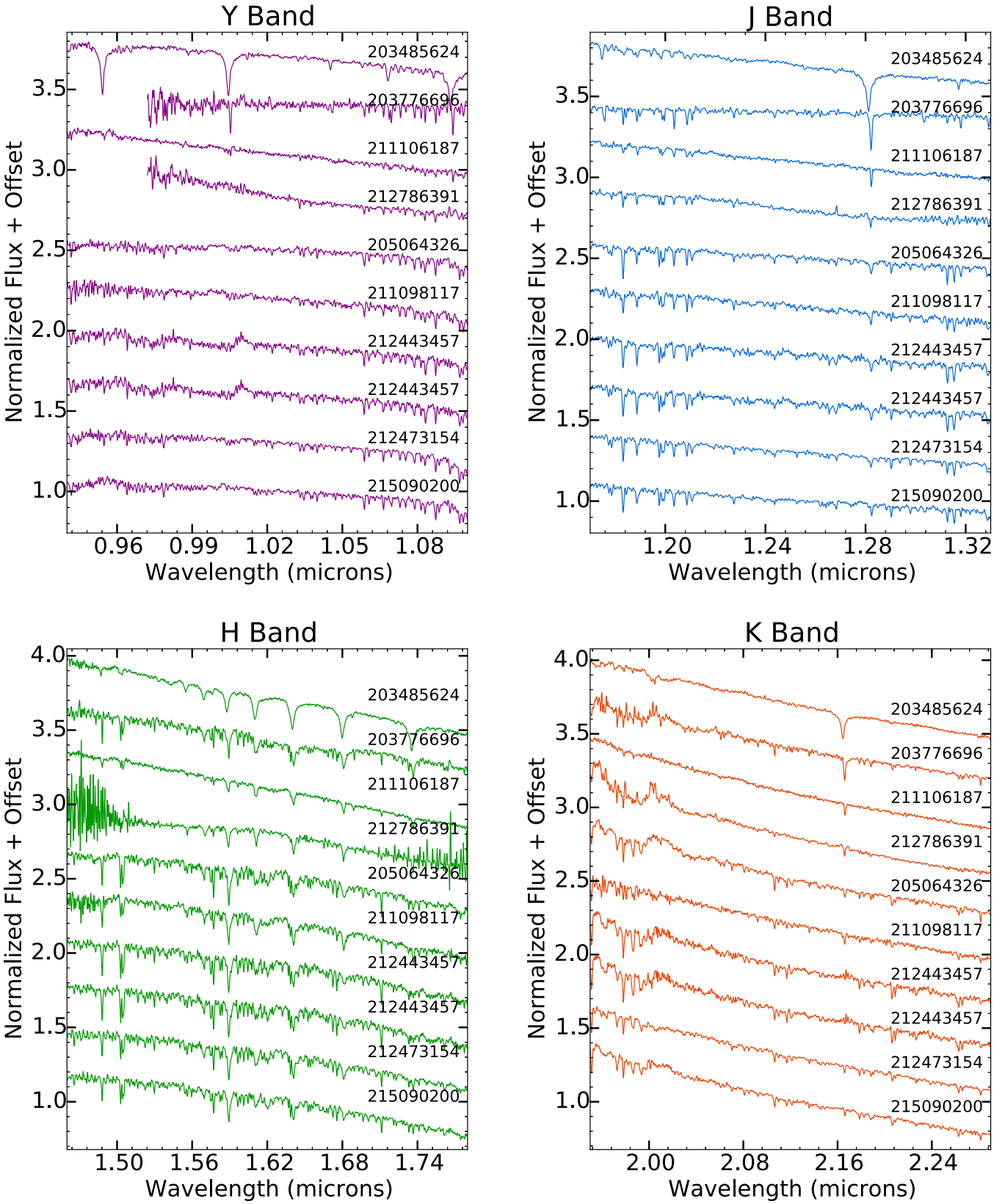

Figure 24. *Y*-band (top left), *J*-band (top right), *H*-band (bottom left), and *K*-band (bottom right) spectra of giant stars with spectral types between F2 and K0. The hottest stars are shown at the top of the plots. Stars with truncated *Y*-band coverage were observed at the Palomar 200″ Hale Telescope using TripleSpec; the other stars were observed at the IRTF using SpeX.

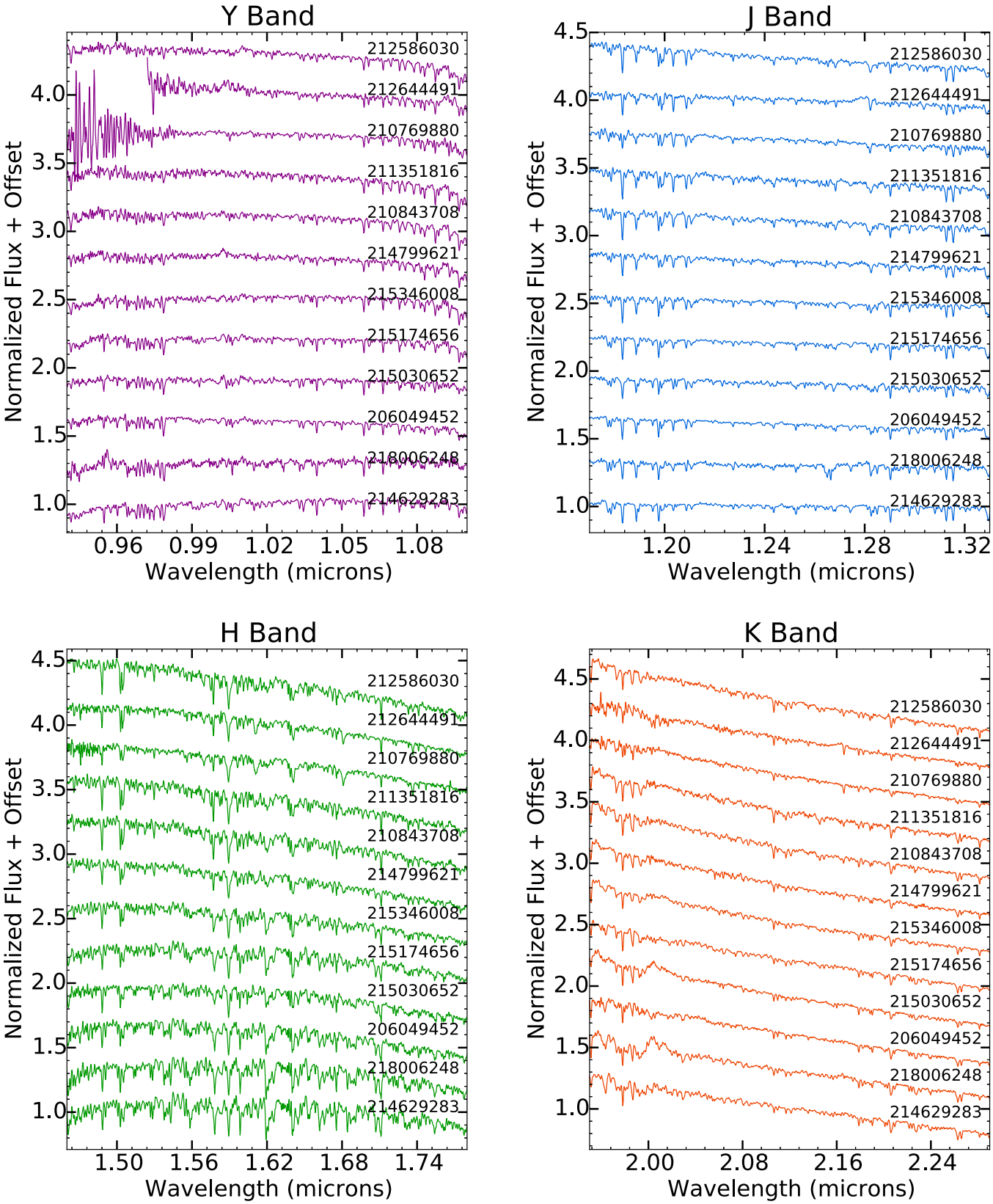

Figure 25. Same as Figure 24 for giant stars with spectral types between K1 and M2.

References

Adams, E. R., Jackson, B., & Endl, M. 2016, AJ, 152, 47
Alam, S., Albareti, F. D., Allende Prieto, C., et al. 2015, ApJS, 219, 12
Allard, F., Homeier, D., & Freytag, B. 2011, in ASP Conf. Ser. 448, 16th Cambridge Workshop on Cool Stars, Stellar Systems, and the Sun, ed. C. Sun, M. K. Johns-Krull, & A. A. Browning (San Francisco, CA: ASP), 91
Barros, S. C. C., Demangeon, O., & Deleuil, M. 2016, A&A, 594, A100
Batalha, N. M., Rowe, J. F., Bryson, S. T., et al. 2013, ApJS, 204, 24
Bensby, T., Feltzing, S., & Oey, M. S. 2014, A&A, 562, A71
Borucki, W. J., Koch, D., Basri, G., et al. 2010, Sci, 327, 977
Borucki, W. J., Koch, D. G., Basri, G., et al. 2011a, ApJ, 728, 117
Borucki, W. J., Koch, D. G., Basri, G., et al. 2011b, ApJ, 736, 19
Boyajian, T. S., von Braun, K., van Belle, G., et al. 2012, ApJ, 757, 112
Brown, T. M., Latham, D. W., Everett, M. E., & Esquerdo, G. A. 2011, AJ, 142, 112
Burke, C. J., Bryson, S. T., Mullally, F., et al. 2014, ApJS, 210, 19
Castelli, F., & Kurucz, R. L. 2004, in Proc. IAU Symp. 210, Modelling of Stellar Atmospheres, ed. N. Piskunov et al. (Cambridge: Cambridge Univ. Press), poster A20
Coşkunoğlu, B., Ak, S., Bilir, S., et al. 2011, MNRAS, 412, 1237
Cohen, M., Wheaton, W. A., & Megeath, S. T. 2003, AJ, 126, 1090
Collier Cameron, A., Wilson, D. M., West, R. G., et al. 2007, MNRAS, 380, 1230
Covey, K. R., Lada, C. J., Román-Zúñiga, C., et al. 2010, ApJ, 722, 971
Crossfield, I. J. M., Ciardi, D. R., Petigura, E., et al. 2016, ApJS, 226, 7
Cushing, M. C., Vacca, W. D., & Rayner, J. T. 2004, PASP, 116, 362
Demarque, P., Woo, J.-H., Kim, Y.-C., & Yi, S. K. 2004, ApJS, 155, 667
Dotter, A., Chaboyer, B., Jevremović, D., et al. 2008, ApJS, 178, 89
Dressing, C. D., & Charbonneau, D. 2013, ApJ, 767, 95
Dressing, C. D., & Charbonneau, D. 2015, ApJ, 807, 45
Feiden, G. A., Chaboyer, B., & Dotter, A. 2011, ApJL, 740, L25
Foreman-Mackey, D., Montet, B. T., Hogg, D. W., et al. 2015, ApJ, 806, 215
Gaidos, E. 2013, ApJ, 770, 90
Gaidos, E., Anderson, D. R., Lépine, S., et al. 2014, MNRAS, 437, 3133
Gaidos, E., Mann, A. W., Kraus, A. L., & Ireland, M. 2016, MNRAS, 457, 2877
Girardi, L., Bressan, A., Bertelli, G., & Chiosi, C. 2000, A&AS, 141, 371
Henry, T. J., Jao, W.-C., Subasavage, J. P., et al. 2006, AJ, 132, 2360
Herter, T. L., Henderson, C. P., Wilson, J. C., et al. 2008, Proc. SPIE, 7014, 70140X
Howell, S. B., Sobeck, C., Haas, M., et al. 2014, PASP, 126, 398
Huber, D., Bryson, S. T., Haas, M. R., et al. 2016, ApJS, 224, 2
Huber, D., Silva Aguirre, V., Matthews, J. M., et al. 2014, ApJS, 211, 2
Kordopatis, G., Gilmore, G., Steinmetz, M., et al. 2013, AJ, 146, 134
Luo, A.-L., Zhao, Y.-H., Zhao, G., et al. 2015, RAA, 15, 1095
Mann, A. W., Brewer, J. M., Gaidos, E., Lépine, S., & Hilton, E. J. 2013a, AJ, 145, 52
Mann, A. W., Deacon, N. R., Gaidos, E., et al. 2014, AJ, 147, 160
Mann, A. W., Feiden, G. A., Gaidos, E., Boyajian, T., & von Braun, K. 2015, ApJ, 804, 64
Mann, A. W., Gaidos, E., & Ansdell, M. 2013b, ApJ, 779, 188
Mann, A. W., Gaidos, E., Lépine, S., & Hilton, E. J. 2012, ApJ, 753, 90
Marigo, P., & Girardi, L. 2007, A&A, 469, 239
Marigo, P., Girardi, L., Bressan, A., et al. 2008, A&A, 482, 883
Martinez, A. O., Crossfield, I. J. M., Schlieder, J. E. M., et al. 2017, ApJ, in press (arXiv:1701.00588)
Montet, B. T., Morton, T. D., Foreman-Mackey, D., et al. 2015, ApJ, 809, 25
Morton, T. D., & Swift, J. 2014, ApJ, 791, 10
Muirhead, P. S., Becker, J., Feiden, G. A., et al. 2014, ApJS, 213, 5
Muirhead, P. S., Hamren, K., Schlawin, E., et al. 2012, ApJL, 750, L37
Newton, E. R., Charbonneau, D., Irwin, J., et al. 2014, AJ, 147, 20
Newton, E. R., Charbonneau, D., Irwin, J., & Mann, A. W. 2015, ApJ, 800, 85
Osborn, H. P., Santerne, A., Barros, S. C. C., et al. 2016, A&A, submitted (arXiv:1605.04291)
Pecaut, M. J., & Mamajek, E. E. 2013, ApJS, 208, 9
Pope, B. J. S., Parviainen, H., & Aigrain, S. 2016, MNRAS, 461, 3399
Rayner, J. T., Cushing, M. C., & Vacca, W. D. 2009, ApJS, 185, 289
Rayner, J. T., Onaka, P. M., Cushing, M. C., & Vacca, W. D. 2004, Proc. SPIE, 5492, 1498
Rayner, J. T., Toomey, D. W., Onaka, P. M., et al. 2003, PASP, 115, 362
Roeser, S., Demleitner, M., & Schilbach, E. 2010, AJ, 139, 2440
Rojas-Ayala, B., Covey, K. R., Muirhead, P. S., & Lloyd, J. P. 2012, ApJ, 748, 93
Sharma, S., Bland-Hawthorn, J., Johnston, K. V., & Binney, J. 2011, ApJ, 730, 3
Vacca, W. D., Cushing, M. C., & Rayner, J. T. 2003, PASP, 115, 389
Van Cleve, J. E., & Caldwell, D. A. 2016, Kepler Instrument Handbook, KSCI-19033-002 (Baltimore, MD: STSci) https://archive.stsci.edu/kepler/documents.html
Van Cleve, J. E., Howell, S. B., Smith, J. C., et al. 2016, PASP, 128, 075002
Vanderburg, A., Latham, D. W., Buchhave, L. A., et al. 2016, ApJS, 222, 14
van Leeuwen, F. 2007, A&A, 474, 653
Winters, J. G., Henry, T. J., Lurie, J. C., et al. 2015, AJ, 149, 5